Research
A SCIENCE PARTNER JOURNAL

RESEARCH ARTICLE

Inhibiting Transcriptional Hub: A Phase-Separating RNA Polymerase Alpha Subunit as a First-in-Class Agrochemical Target against *Xanthomonas*

Xiaoguo Wang[1,2†], Ting Liu[1†], Jianzhuan Li[1], Chunni Zhao[1], Deyu Hu[1*], and Runjiang Song[1*]

[1]State Key Laboratory of Green Pesticide, Center for R&D of Fine Chemicals, Guizhou University, Guiyang 550025, China. [2]Public Course Teaching Department, Qiannan Medical College for Nationalities, Duyun 558000, China.

*Address correspondence to: dyhu@gzu.edu.cn (D.H.); songrj@gzu.edu.cn (R.S.)
†These authors contributed equally to this work.

Citation: Wang X, Liu T, Li J, Zhao C, Hu D, Song R. Inhibiting Transcriptional Hub: A Phase-Separating RNA Polymerase Alpha Subunit as a First-in-Class Agrochemical Target against *Xanthomonas*. *Research* 2026;9:Article 1222. https://doi.org/10.34133/research.1222

Submitted 3 November 2025
Revised 13 February 2026
Accepted 7 March 2026
Published 31 March 2026

Copyright © 2026 Xiaoguo Wang et al. Exclusive licensee Science and Technology Review Publishing House. No claim to original U.S. Government Works. Distributed under a Creative Commons Attribution License (CC BY 4.0).

Effective management of plant pathogenic bacteria faces major challenges, including rapidly evolving bacterial resistance, environmental risks associated with traditional copper-based agrochemicals, and the scarcity of new antibacterial targets. Recently, liquid–liquid phase separation (LLPS) has been extensively demonstrated to play crucial roles in microbial biology. However, the use of phase-separating proteins as targets for bactericide development remains unexplored. Herein, we report the first syringic acid derivative, $\mathbf{C_{31}}$, that targets the alpha subunit of RNA polymerase (RpoA) in *Xanthomonas oryzae* pv. *oryzae* (*Xoo*). $\mathbf{C_{31}}$ exhibits exceptional inhibitory activity against *Xoo* (EC_{50} = 0.86 μg/ml, half maximal effective concentration) and maintains a low resistance risk throughout 12 successive passages. Pot experiments show that $\mathbf{C_{31}}$ provides superior control efficacy (59.37%) against rice bacterial leaf blight compared with syringic acid (24.65%) and thiodiazole copper (42.41%), showing sustained efficacy and high crop safety. Mechanistic studies reveal that RpoA and σ^{70} factor undergo LLPS to generate biomolecular condensates that function as "transcriptional hubs", thereby regulating the expression efficiency of global virulence genes and consequently strengthening *Xoo* pathogenicity. $\mathbf{C_{31}}$ binds to the C-terminal domain of RpoA and prevents LLPS initiation and subsequent condensate formation, resulting in antibacterial effects. This study establishes an LLPS-based strategy to control phytopathogenic bacteria.

Introduction

Biomolecular condensates (BMCs) are membraneless intracellular assemblies that organize the cellular space and regulate a vast array of biological processes from transcriptional control and RNA metabolism to signal transduction and stress responses [1]. Their formation is primarily driven by a physical process known as liquid–liquid phase separation (LLPS), in which biomolecules such as proteins and nucleic acids separate from the aqueous cellular milieu into concentrated liquid-like phases [2]. The principle of phase separation extends beyond basic cellular housekeeping to the intricate battle between hosts and pathogens [3,4]. It has been demonstrated that viruses, as obligate intracellular parasites, exploit LLPS to form viral replication factories (known as replication compartments or inclusion bodies [IBs]), which are crucial for viral entry, genome replication, and particle assembly [5]. Although the role of LLPS in viral infections is relatively well-documented, its role in bacterial systems, particularly in pathogenic bacteria, is a burgeoning frontier.

Initially considered a hallmark of eukaryotic cell organization, it is now evident that bacteria harness LLPS to regulate core cellular functions and adapt to environmental stress [6]. The bacterial cytoplasm, characterized by macromolecular crowding, provides a conducive environment for phase separation [7]. In pathogenic bacteria, BMCs have emerged as vital mechanisms for maintaining physicochemical homeostasis under the fluctuating conditions encountered during infection [8]. Studies have begun to connect the formation of these bacterial condensates to the control of essential processes such as chromosome replication, segregation, and cell division [9,10]. This positions LLPS as a fundamental organizational principle in bacteria and a potential contributor to bacterial fitness and virulence. Recent evidence suggests that type III effectors from *Xanthomonas campestris* pv. *campestris* and *Pseudomonas syringae* pv. *tomato* exhibit a propensity for phase separation [11]. Given the pivotal role of type III effectors in the virulence of numerous phytopathogenic bacteria, the targeted disruption of pathogen-driven phase separation in hosts presents a novel and promising opportunity for plant protection. The strategic disruption of pathogenic

condensates has been successfully demonstrated in the context of human diseases [12]. For instance, peptide p1, designed by Liu et al. [13], covalently binds to the Nck protein and obstructs its SH2 domain, thereby dissolving pathogenic condensates in enterohemorrhagic *Escherichia coli* and inhibiting virulence. However, to our knowledge, small-molecule bactericides that specifically target phase-separating proteins in plant pathogenic bacteria remain unexplored.

Plant bacterial diseases caused by *Xanthomonas* species pose a serious threat to agricultural production, particularly for crops such as rice, fruits, and vegetables [14]. The emergence of resistance to conventional copper-based pesticides and agricultural antibiotics, coupled with the scarcity of available antibacterial targets, leads to frequent outbreaks and complicates disease management [15,16]. Therefore, it is critical to discover new bactericidal leads with a unique mode of action. Herein, we report the first application of activity-based protein profiling (ABPP) in identifying the alpha subunit of RNA polymerase (RpoA), a phase-separating protein, in *Xanthomonas oryzae* pv. *oryzae* (*Xoo*), the receptor for syringic acid (SA) derivative $\mathbf{C_{31}}$, which is a small molecule that exhibits excellent antibacterial activity (Fig. 1A). Using homologous recombination, we constructed *RpoA* knockout and complementary strains and systematically investigated their effects on *Xoo* pathogenicity and virulence. We revealed that RpoA mediates *Xoo* virulence by forming BMCs with σ^{70} via LLPS, which orchestrates a σ-factor-mediated transcriptional network to promote the expression of key pathogenicity factors such as biofilm formation, extracellular polysaccharide (EPS) production, and motility. $\mathbf{C_{31}}$ was shown to exert its antibacterial effect by inhibiting the generation of *Xoo* RpoA–σ^{70} droplets. This study provides a molecular foundation and a practical lead structure for the development of agrochemicals that target phytobacterial phase separation.

Results

Design and synthesis of antibacterial SA derivatives

SA, a natural phenolic acid, shows broad-spectrum antimicrobial activity and possesses advantageous properties, including low toxicity, ready biodegradability, and low propensity for resistance development, making it a highly promising scaffold for antimicrobial agents [17,18]. Nevertheless, the systematic structural derivatization of SA to obtain highly active antimicrobial molecules remains relatively limited. In recent years, allicin-inspired disulfide units have attracted considerable interest for bactericide design [19,20]. For example, Li et al. [21] reported a series of compounds incorporating a 1,3,4-oxadiazole-based asymmetric disulfide motif, which exhibited excellent inhibitory activity against various phytopathogenic bacteria and the capacity to activate plant systemic acquired resistance. On this basis, a molecular hybridization strategy was employed to conjugate the SA core with a disulfide-containing 1,3,4-oxadiazole moiety to construct novel antimicrobial compound C (Fig. 1A). We devised a 3-step synthetic route to access the target products $\mathbf{C_1}$ to $\mathbf{C_{34}}$ (Fig. S1). The key transformations involved esterification, etherification, Koparir [22] synthesis of the 1,3,4-oxadiazole-2-thiol intermediate, and a 2,3-dicyano-5,6-dichlorobenzoquinone (DDQ)-mediated oxidative C–S coupling reaction for disulfide formation. This final oxidative coupling step proceeded reliably, demonstrating good functional group tolerance and affording the target compounds in moderate to good yields (47.5% to 77.4%), which were influenced by the structure of the thiol component. All intermediate and final compounds were thoroughly characterized using ^{1}H nuclear magnetic resonance (NMR), ^{13}C NMR, and high-resolution mass spectrometry to confirm their structural integrity (Supplementary Materials I).

$\mathbf{C_{31}}$ shows promising in vitro and in vivo bactericidal activity against *Xoo*

Following the synthesis of the target molecules, we systematically evaluated their inhibitory activity against *Xoo*. The initial assessment of the in vitro activity of compounds $\mathbf{C_1}$ to $\mathbf{C_{34}}$ against *Xoo* was performed using the classical turbidimetric method, with the parent compound SA and commercial thiodiazole copper (TC) as positive controls. As shown in Table 1, for compounds containing the same ethyl disulfide moiety, the introduction of either aliphatic chains ($\mathbf{C_1}$ to $\mathbf{C_6}$) or aromatic rings ($\mathbf{C_7}$ to $\mathbf{C_{11}}$) into the parent structure resulted in the most substantial enhancement of antibacterial activity, with short-chain aliphatic hydrocarbons showing the strongest effect. This prompted further exploration of disulfide substituents while retaining the parent benzyloxy group. Compared with aliphatic chains, the introduction of aromatic hydrocarbons (e.g., $\mathbf{C_{18}}$) improved activity, with benzyl substitution notably enhancing the inhibitory effect. This was corroborated by comparing compound $\mathbf{C_{19}}$ (4-Cl-phenyl, EC_{50} = 2.76 μg/ml) and $\mathbf{C_{26}}$ (4-Cl-benzyl, EC_{50} = 1.98 μg/ml). Consequently, optimization efforts focused on the use of benzyl disulfide derivatives. Introducing multiple substituents on the benzene ring reduced anti-*Xoo* activity, as observed for $\mathbf{C_{23}}$ (4-CH_3, EC_{50} = 1.89 μg/ml) and $\mathbf{C_{24}}$ (2,4,6-tri-CH_3-benzyl, EC_{50} = 4.46 μg/ml). Extending the chain length between the disulfide bond and the benzene ring markedly enhanced inhibition against *Xoo* (Fig. 1B and C). Among all derivatives, $\mathbf{C_{31}}$ exhibited the highest activity with an EC_{50} value of 0.86 μg/ml, which is only 1/98 that of SA (EC_{50} = 84.68 μg/ml) and 1/72 that of TC (EC_{50} = 62.27 μg/ml). These results indicate that $\mathbf{C_{31}}$ possesses excellent in vitro inhibitory activity against *Xoo*, warranting further evaluation.

To more accurately assess the efficacy of $\mathbf{C_{31}}$, we conducted in vivo pot experiments using the leaf-clipping method to evaluate its control of bacterial leaf blight (BLB) caused by *Xoo* in rice. The results showed severe disease symptoms on rice leaves of both the blank control and SA-treated groups (Fig. 1D and E). In contrast, treatment with 200 μg/ml $\mathbf{C_{31}}$ significantly alleviated BLB symptoms, achieving a disease control efficacy of 59.37% in the susceptible rice variety 'Fengyouxiangzhan', which was superior to that of SA (24.65%) and the commercial bactericide TC (42.41%). $\mathbf{C_{31}}$ also exhibited substantial protective activity (52.72% control efficacy) against BLB on another widely cultivated variety, 'Bōyōu 903' (Fig. S2), suggesting that its effectiveness is not limited to a single genetic background. These findings are consistent with the in vitro antibacterial activity of $\mathbf{C_{31}}$, supporting its outstanding and broad-spectrum potential for combating *Xoo* infections.

Identification of 3 potential receptors for $\mathbf{C_{31}}$ via the ABPP technique

Given the potent antibacterial activity of compound $\mathbf{C_{31}}$ against *Xoo*, we used ABPP to investigate its molecular targets. We first explored suitable sites on the $\mathbf{C_{31}}$ scaffold for introducing a probe group (Fig. 1F). Based on its structure, we synthesized $\mathbf{C_{35}}$ (where the 4-position methoxy group on the SA aromatic

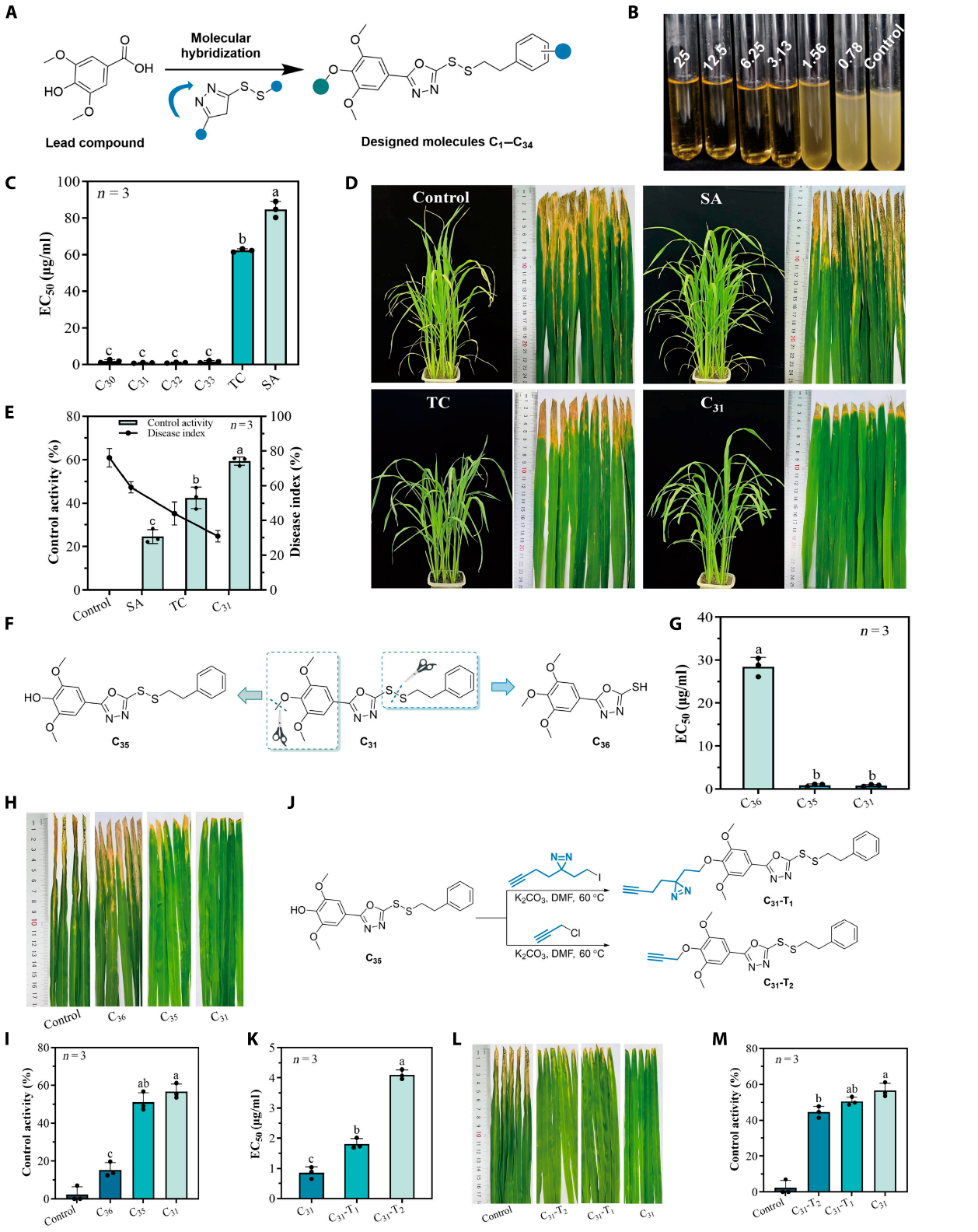
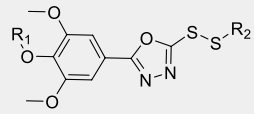


Fig. 1. Identification and validation of **C_{31}** as a potent anti-*Xanthomonas oryzae* pv. *oryzae* (anti-*Xoo*) agent. (A) Schematic diagram of the design strategy for the target derivatives. (B and C) In vitro anti-*Xoo* activity of the synthesized derivatives. (D and E) In vivo bioactivity of **C_{31}** against *Xoo*. (F) The chemical structures of the designed probes. (G to I) The in vitro and in vivo activities of compounds **C_{31}**, **C_{35}**, and **C_{36}** against *Xoo*. (J) Synthetic route for probes. (K to M) The in vitro and in vivo activities of probes. (C, E, G, I, K, and M) Error bars represent the mean ± standard error (SE). Different letters indicate statistically significant differences as determined using one-way analysis of variance (ANOVA) (IBM SPSS Statistics 24) followed by a least significant difference (LSD) post hoc test ($P < 0.05$). TC, thiodiazole copper; SA, syringic acid; DMF, dimethylformamide.

Table 1. Antibacterial efficacy of $\mathbf{C_1}$ to $\mathbf{C_{34}}$ compounds against *Xoo* in vitro. Data are presented as mean ± standard deviation. $n = 3$. Syringic acid (SA, 92%) and thiodiazole copper (TC, 20%) were used as positive controls.



Compd.	R_1	R_2	Inhibition ratio (%) 25 μg/ml	Inhibition ratio (%) 12.5 μg/ml	Regression equation	EC_{50} (μg/ml)
$\mathbf{C_1}$	Methyl	Ethyl	100	91.08 ± 1.37	$y = 2.72x + 3.40$	3.89 ± 0.21
$\mathbf{C_2}$	Ethyl	Ethyl	93.50 ± 3.06	89.32 ± 3.72	$y = 2.79x + 2.94$	5.48 ± 1.34
$\mathbf{C_3}$	Propyl	Ethyl	92.04 ± 3.29	82.70 ± 2.11	$y = 2.92x + 2.65$	6.26 ± 0.19
$\mathbf{C_4}$	Isopropyl	Ethyl	86.12 ± 1.46	74.64 ± 2.48	$y = 2.85x + 2.49$	7.60 ± 0.64
$\mathbf{C_5}$	Butyl	Ethyl	88.43 ± 1.94	78.65 ± 2.63	$y = 3.04x + 2.56$	6.74 ± 0.37
$\mathbf{C_6}$	Pentyl	Ethyl	85.68 ± 2.84	74.38 ± 2.92	$y = 2.96x + 2.41$	7.18 ± 0.28
$\mathbf{C_7}$	Benzyl	Ethyl	77.89 ± 3.13	69.06 ± 2.23	$y = 2.99x + 2.14$	9.06 ± 1.51
$\mathbf{C_8}$	4-F-benzyl	Ethyl	91.39 ± 2.68	65.64 ± 3.92	$y = 3.03x + 2.14$	8.57 ± 0.69
$\mathbf{C_9}$	4-Cl-benzyl	Ethyl	68.29 ± 1.42	54.98 ± 2.08	$y = 1.46x + 3.50$	10.20 ± 0.89
$\mathbf{C_{10}}$	4-Br-benzyl	Ethyl	62.62 ± 2.19	51.81 ± 1.89	$y = 1.66x + 3.19$	11.59 ± 0.67
$\mathbf{C_{11}}$	4-CH_3-benzyl	Ethyl	58.41 ± 2.43	48.77 ± 2.78	$y = 1.98x + 2.63$	14.60 ± 1.33
$\mathbf{C_{12}}$	Methyl	Propyl	96.40 ± 2.11	92.90 ± 3.26	$y = 2.49x + 3.99$	2.68 ± 0.15
$\mathbf{C_{13}}$	Methyl	Butyl	92.74 ± 1.76	86.91 ± 2.70	$y = 3.11x + 3.10$	4.08 ± 0.43
$\mathbf{C_{14}}$	Methyl	Pentyl	92.90 ± 2.57	88.23 ± 2.45	$y = 2.71x + 3.02$	5.09 ± 0.30
$\mathbf{C_{15}}$	Methyl	Hexyl	83.68 ± 2.19	74.18 ± 1.98	$y = 1.54x + 3.78$	6.04 ± 0.16
$\mathbf{C_{16}}$	Methyl	Cyclopentyl	89.54 ± 2.91	83.51 ± 2.81	$y = 2.50x + 3.28$	5.47 ± 0.66
$\mathbf{C_{17}}$	Methyl	Cyclohexyl	77.06 ± 3.27	59.68 ± 2.08	$y = 1.53x + 3.60$	8.06 ± 0.72
$\mathbf{C_{18}}$	Methyl	Benzyl	99.25 ± 1.30	90.57 ± 1.37	$y = 1.91x + 4.26$	2.27 ± 0.17
$\mathbf{C_{19}}$	Methyl	4-Cl-phenyl	92.47 ± 2.12	80.12 ± 3.19	$y = 1.70x + 4.18$	2.76 ± 0.25
$\mathbf{C_{20}}$	Methyl	2-CH_3-phenyl	86.03 ± 1.63	69.16 ± 1.58	$y = 1.39x + 4.06$	4.79 ± 0.21
$\mathbf{C_{21}}$	Methyl	2-CH_3-benzyl	95.19 ± 4.20	87.93 ± 4.07	$y = 3.38x + 3.34$	2.68 ± 0.41
$\mathbf{C_{22}}$	Methyl	3-CH_3-benzyl	93.05 ± 2.86	79.46 ± 0.79	$y = 1.92x + 3.91$	3.79 ± 0.23
$\mathbf{C_{23}}$	Methyl	4-CH_3-benzyl	97.24 ± 2.62	89.45 ± 4.41	$y = 3.10x + 3.85$	1.89 ± 0.42
$\mathbf{C_{24}}$	Methyl	2,4,6-triCH_3-benzyl	88.86 ± 3.21	71.74 ± 3.62	$y = 2.10x + 3.52$	4.46 ± 0.62
$\mathbf{C_{25}}$	Methyl	4-F-benzyl	98.07 ± 1.72	92.32 ± 3.95	$y = 3.05x + 4.09$	1.75 ± 0.23
$\mathbf{C_{26}}$	Methyl	4-Cl-benzyl	93.82 ± 4.18	83.15 ± 4.08	$y = 1.85x + 4.40$	1.98 ± 0.52
$\mathbf{C_{27}}$	Methyl	2,4-diCl-benzyl	84.17 ± 3.01	69.13 ± 3.67	$y = 1.30x + 4.29$	2.65 ± 0.79
$\mathbf{C_{28}}$	Methyl	4-Br-benzyl	92.11 ± 2.37	78.51 ± 4.54	$y = 1.52x + 4.44$	2.09 ± 0.91
$\mathbf{C_{29}}$	Methyl	4-$(CH_3)_3$C-benzyl	85.97 ± 2.12	67.33 ± 2.68	$y = 0.92x + 4.68$	2.52 ± 0.82
$\mathbf{C_{30}}$	Methyl	1-Phenylethyl	100	90.87 ± 4.02	$y = 1.64x + 4.58$	1.86 ± 0.79
$\mathbf{C_{31}}$	Methyl	CH_2-benzyl	100	96.59 ± 2.67	$y = 2.39x + 4.96$	0.86 ± 0.20
$\mathbf{C_{32}}$	Methyl	2-phenylpropyl	100	94.64 ± 2.78	$y = 2.49x + 4.76$	0.94 ± 0.27
$\mathbf{C_{33}}$	Methyl	CH_2CH_2-benzyl	92.61 ± 2.79	88.67 ± 2.19	$y = 4.19x + 3.54$	1.53 ± 0.60
$\mathbf{C_{34}}$	Methyl	2-CH_3-furan	90.61 ± 4.78	79.27 ± 3.62	$y = 1.45x + 4.53$	1.99 ± 0.72
SA	/	/	13.04 ± 1.67	2.44 ± 0.39	$y = 2.11x + 0.88$	84.68 ± 4.40
TC	/	/	20.31 ± 1.09	9.27 ± 0.89	$y = 1.79x + 1.79$	62.27 ± 0.91

Xoo, *Xanthomonas oryzae* pv. *oryzae*

ring was replaced by a hydroxyl group) and $\mathbf{C_{36}}$ (which lacks the disulfide moiety linked to the 1,3,4-oxadiazole part; the synthetic route and structural characterization data are shown in Fig. S3 and Supplementary Materials I). Bioactivity tests revealed that $\mathbf{C_{35}}$ exhibited an EC_{50} value of 0.90 μg/ml toward *Xoo* and a control efficacy of 51.03% against rice BLB,

comparable to those of $\mathbf{C_{31}}$ (EC_{50} = 0.86 μg/ml, control efficacy 56.64%). In contrast, $\mathbf{C_{36}}$ (EC_{50} = 28.45 μg/ml, control efficacy 15.30%) showed a significantly reduced activity (Fig. 1G to I). These data indicate that the disulfide moiety is a crucial pharmacophore for maintaining bioactivity, thus permitting the introduction of a probe group at the *para*-position of the SA aromatic ring.

To synthesize the chemical probes, compound $\mathbf{C_{35}}$ was reacted with commercially available 3-(3-butyn-1-yl)-3-(2-iodoethyl)-3*H*-diazirine (CAS: 1450754-38-7) and 3-chloropropyne (CAS: 624-65-7), respectively, in the presence of K_2CO_3 in dimethylformamide at 60 °C, yielding the target molecules $\mathbf{C_{31}}$-$\mathbf{T_1}$ and $\mathbf{C_{31}}$-$\mathbf{T_2}$ (Fig. 1J). The structural accuracy of the probes was confirmed using ^{1}H NMR, ^{13}C NMR spectroscopy, and high-resolution mass spectrometry (Figs. S123 to S128). Considering that the introduction of the probe group might have affected the efficacy of the parent compound, the antibacterial activities of $\mathbf{C_{31}}$-$\mathbf{T_1}$ and $\mathbf{C_{31}}$-$\mathbf{T_2}$ were re-evaluated (Fig. 1K to M). Both probes demonstrated low EC_{50} values (1.81 and 4.10 μg/ml, respectively) and good control efficacy against rice BLB (50.57% and 44.54%, respectively), validating their suitability as activity-based probes for subsequent target identification.

Using the obtained probes $\mathbf{C_{31}}$-$\mathbf{T_1}$ and $\mathbf{C_{31}}$-$\mathbf{T_2}$, we further executed the ABPP workflow, which primarily involved specific labeling, concentration dependence, competitive inhibition, and pull-down analyses (Fig. 2A). At a concentration of 50 μM, both $\mathbf{C_{31}}$-$\mathbf{T_1}$ and $\mathbf{C_{31}}$-$\mathbf{T_2}$ captured similar protein bands within the 29- to 38-kDa range (Fig. 2B), suggesting a consistent labeling mechanism aligned with their comparable EC_{50} values. Because of its superior photo-cross-linking efficiency and stability conferred by the acridinyl group [23], $\mathbf{C_{31}}$-$\mathbf{T_1}$ was selected as a representative probe for subsequent experiments. This probe exhibited dose-dependent enhancement of labeling from 0 to 100 μM, indicating specific binding (Fig. 2C). In competition experiments, preincubation with $\mathbf{C_{31}}$ dose-dependently reduced the labeling efficiency of $\mathbf{C_{31}}$-$\mathbf{T_1}$ (Fig. 2D), indicating that both compounds share identical binding sites.

To further identify the targets, we performed pull-down enrichment using $\mathbf{C_{31}}$-$\mathbf{T_1}$ on *Xoo* lysates, followed by copper(I)-catalyzed azide-alkyne cycloaddition-mediated biotin conjugation, streptavidin bead purification, and liquid chromatography–tandem mass spectrometry analysis. No apparent enrichment was observed in the dimethyl sulfoxide (DMSO) control group (Fig. 2E), whereas 3 potential target proteins within the expected molecular weight range were identified in the $\mathbf{C_{31}}$-$\mathbf{T_1}$ treatment group (Fig. 2F and Table S2): RpoA (involved in DNA transcription regulation), elongation factor Ts (Tsf, facilitates polypeptide chain elongation), and disulfide interchange protein DsbA (associated with the antioxidant stress response). Reverse transcription quantitative polymerase chain reaction (RT-qPCR) analysis revealed significant down-regulation in the expression of genes encoding the candidate targets RpoA, Tsf, and DsbA. Compared with that of the reference gene *16S rRNA*, their transcript levels were reduced by 89.17%, 51.90%, and 33.19%, respectively (Fig. 2G). These results provide preliminary evidence that these 3 proteins are potential targets of $\mathbf{C_{31}}$.

RpoA-encoding gene knockout severely impairs *Xoo* pathogenicity and virulence-associated factors

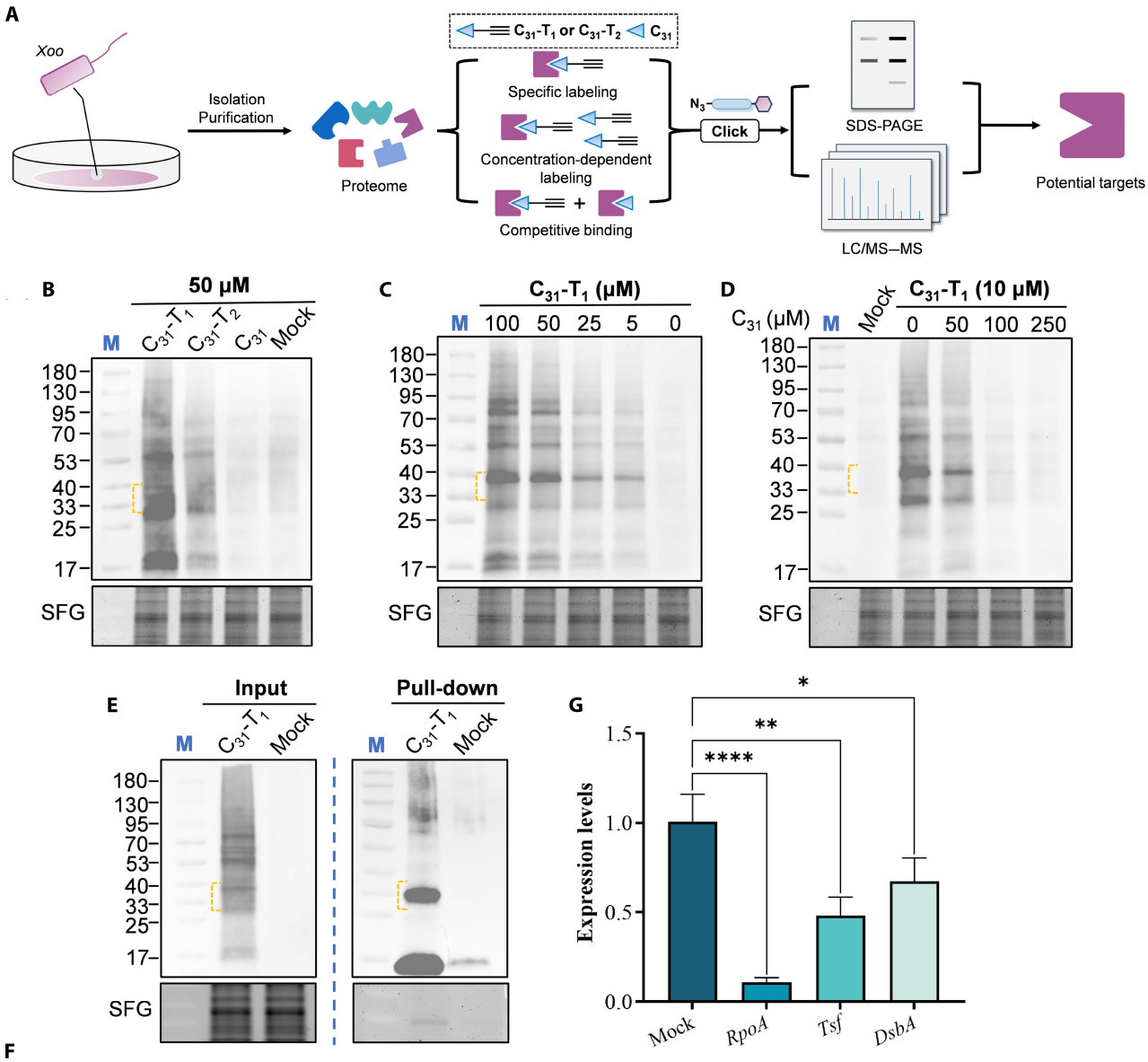
To investigate the impact of the identified target proteins on *Xoo* pathogenicity, we successfully constructed knockout mutants for the target genes *RpoA*, *Tsf*, and *DsbA* (designated as ΔRpoA, ΔTsf, and ΔDsbA, respectively) using a markerless homologous double-crossover recombination method (Fig. 3A and Fig. S4). Pathogenicity analysis of the mutants in rice (Fig. 3B and C) showed that compared to that of the wild-type $PXO99^A$ (lesion length 16.40 cm), the pathogenicity of ΔRpoA was significantly reduced (lesion length 2.06 cm, a decrease of 87.4%), while ΔTsf (12.60 cm) and ΔDsbA (13.16 cm) exhibited only slight reductions. Furthermore, we evaluated the ability of the mutant strains to induce a hypersensitive response (HR) in *Nicotiana benthamiana*. HR is a rapid defense mechanism triggered in plants upon pathogen infection and typically manifests as the formation of localized necrotic spots [24]. The results showed that ΔDsbA induced necrotic spots similar to those of the wild type, appearing brown with clear boundaries (Fig. 3D). ΔTsf induced relatively small necrotic spots, and no obvious necrotic spots were observed in ΔRpoA. These results indicate that the absence of *RpoA* severely impairs bacterial pathogenicity and host interactions, whereas the loss of *Tsf* and *DsbA* only partially affects pathogenicity.

Biofilm formation is a critical capability of pathogens to colonize host or abiotic surfaces, enhancing bacterial adhesion and tolerance to environmental stress [25]. Crystal violet staining results (Fig. 3E and F) showed that the biofilm formation ability of the ΔRpoA mutant decreased by 56.50% compared to that of the wild type, a reduction significantly greater than that observed in the ΔTsf and ΔDsbA mutants. EPS is an important virulence factor that confers the typical mucoid colony phenotype and plays a key role in the pathogenic process [26]. Colony morphology observations revealed that ΔRpoA colonies became flat and dull, while ΔTsf and ΔDsbA maintained a plump morphology similar to that of the wild type (Fig. 3G). Quantitative analysis further confirmed a 41.6% decrease in EPS production in ΔRpoA, with no apparent changes in other mutants (Fig. 3H).

Bacterial motility and growth are important virulence traits in host infection [27]. A swimming assay showed that the diffusion diameter of ΔRpoA (9.03 mm) was reduced by 36.5% compared with that of the wild type (14.23 mm), while other mutants were less affected (Fig. 3I and J). Growth curves indicated that ΔRpoA exhibited a lag phase prolonged by 5 h and a considerably reduced growth rate, whereas ΔTsf and ΔDsbA only showed mild growth delays (Fig. 3K). During plant infections, *Xanthomonas* often encounters reactive oxygen species generated by the host immune responses [28]. In a medium containing 0.1 mM H_2O_2, both wild-type and mutant strains grew normally, indicating that these mutations did not substantially affect bacterial reactive oxygen species tolerance (Fig. 3L). Collectively, these findings suggested that RpoA plays a central role in regulating bacterial pathogenicity, energy metabolism, and physiological functions.

Complementation of *RpoA* markedly restores *Xoo* pathogenicity and virulence factors

To confirm that the observed pathogenic phenotypic changes were directly caused by the deletion of the RpoA-encoding gene, we constructed the complementary strain CΔRpoA. This strain was generated using the pBBR1MCS-2 vector and $PXO99^A$ genomic DNA as templates, with complementary primers containing promoter sequences to amplify the target gene (Fig. S5), and its virulence-related functions were validated. Experimental



Protein ID	Protein names	Gene names	Intensity	
			Mock	C_{31}-T_1
B2SQT4|RPOA_XANOP	DNA-directed RNA polymerase subunit alpha	PXO_04496	0	167.77
B2SQZ9|EFTS_XANOP	Elongation factor Ts	PXO_01131	0	350.94
A0A0K0GHC5_XANOP	Disulfide interchange protein DsbA	PXO_04434	0	631.39

Fig. 2. Target identification of probes in *Xoo* using an activity-based protein profiling (ABPP) strategy. (A) Workflow for cellular target enrichment and identification by ABPP (sodium dodecyl sulfate–polyacrylamide gel electrophoresis [SDS–PAGE] and liquid chromatography–tandem mass spectrometry [LC–MS/MS]). (B) Specific binding of probes **C_{31}-T_1** and **C_{31}-T_2** to an unknown target within the 29- to 38-kDa range in *Xoo* cell lysates. This binding could not be observed with compound **C_{31}** or dimethyl sulfoxide treatment. (C) Concentration-dependent labeling of the target by **C_{31}-T_1**. (D) Dose-dependent inhibition of probe **C_{31}-T_1** labeling in *Xoo* cell lysates by pretreatment with compound **C_{31}**. (E and F) Schematic diagram of target enrichment and pull-down assay using the probe **C_{31}-T_1** in *Xoo* cells. (G) Relative expression of candidate target genes in *Xoo* after **C_{31}** treatment. Stain-free gel (SFG) was used as a loading control to confirm equal protein amounts across lanes. Statistical significance between means was determined by a Student *t* test, with significance levels denoted as $^*P < 0.05$, $^{**}P < 0.01$, and $^{***}P < 0.001$; ns, not significant.

results (Fig. 4A) showed that the biofilm formation of ΔRpoA was significantly reduced to 0.29 at 45 h (compared to 0.89 for the wild-type PXO99^A). The complementary strain CΔRpoA restored biofilm formation to 85.86% of the wild-type level and shortened the lag phase by 3.2 h. Further studies revealed that at concentrations below 2.0 × EC_{50}, compound **C_{31}** had

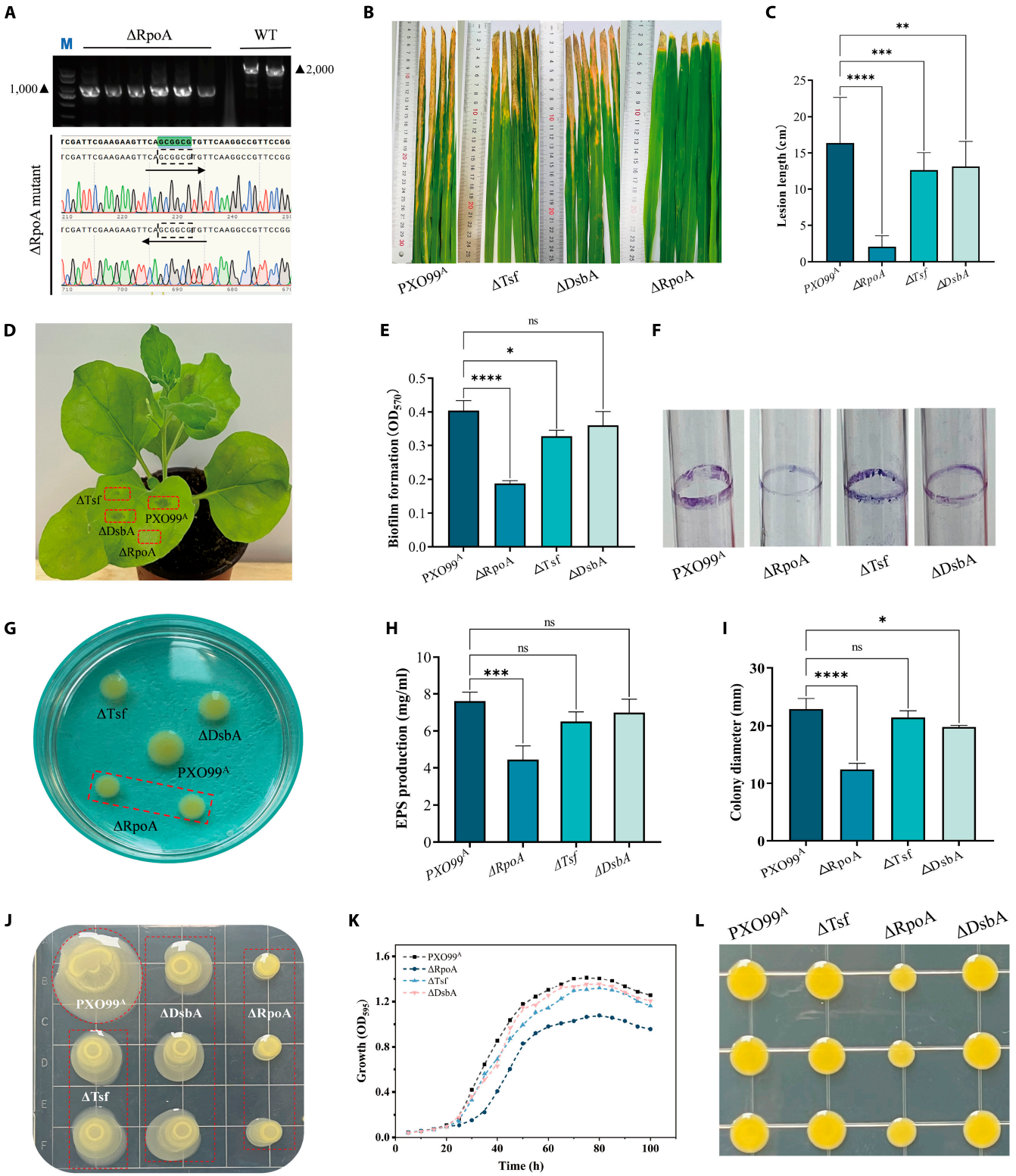


Fig. 3. Deletion of candidate target protein-encoding genes impairs virulence and associated phenotypes in *Xoo*. (A) Validation of the *RpoA* gene knockout using polymerase chain reaction (PCR) and DNA sequencing. (B and C) Pathogenicity of the wild-type (PXO99^A), ΔRpoA, ΔTsf, and ΔDsbA mutants on rice. Lesion lengths were measured at 14 d postinoculation. (D) Hypersensitive response induced by mutant strains in tobacco. (E and F) Biofilm formation quantified using crystal violet staining. (G and H) Extracellular polysaccharide (EPS) production assessed using quantification and visual observation. (I and J) Bacterial motility evaluated using a swimming assay and colony expansion. (K) In vitro growth curves of the mutant strains in nutrient broth. (L) Oxidative stress tolerance of the mutants on nutrient agar (NA) plates supplemented with 0.1 mM H_2O_2. (C, E, H, and I) Error bars represent mean ± SE. Statistical significance between means was determined using a Student *t* test, with significance levels denoted as $^*P < 0.05$, $^{**}P < 0.01$, $^{***}P < 0.001$, and $^{****}P < 0.0001$; ns, not significant. Experiments were repeated at least 3 times, and the sample size for each data point is indicated in the corresponding figure. WT, wild type.

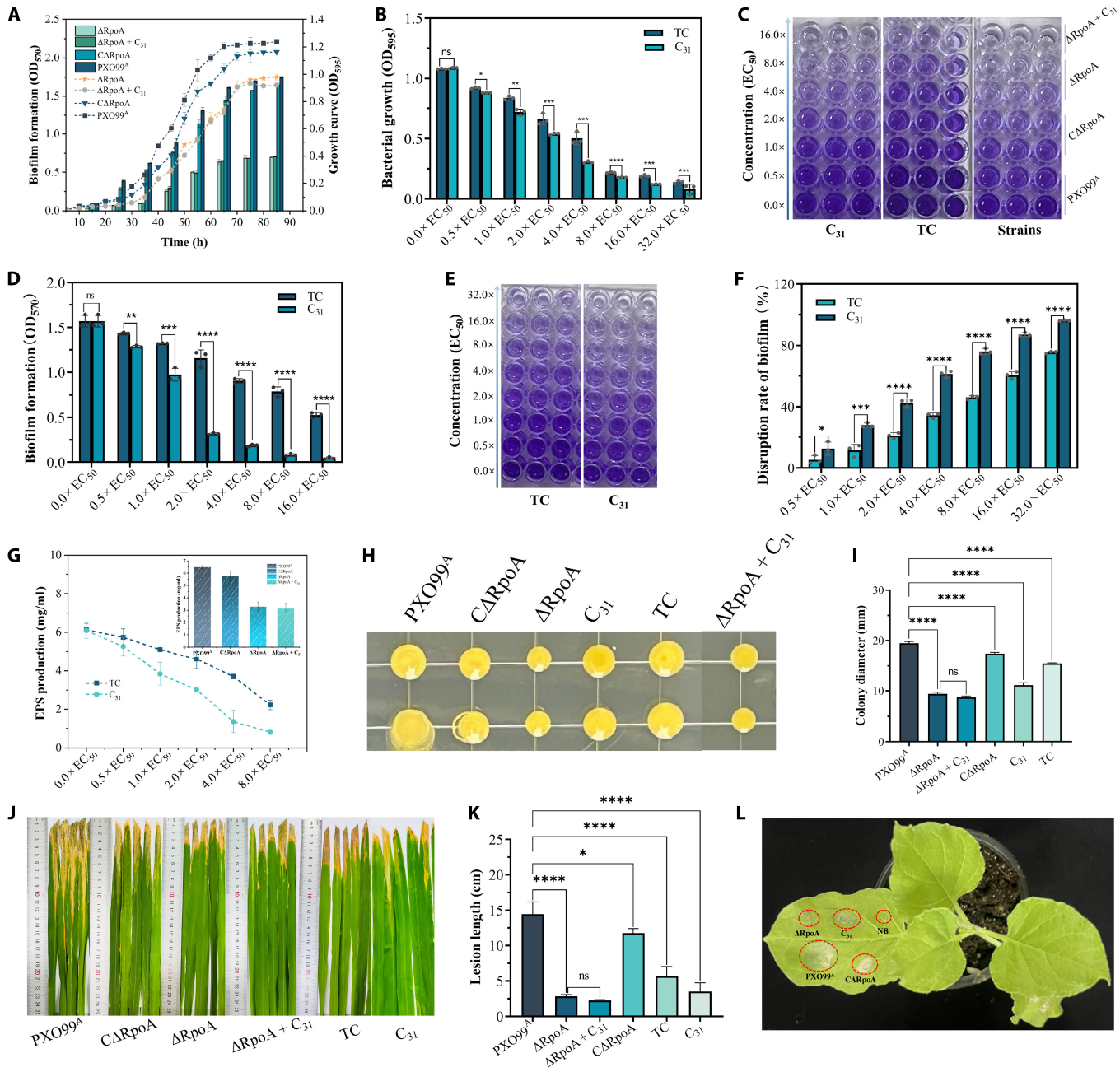


Fig. 4. Genetic complementation of ΔRpoA and inhibition of virulence by $\mathbf{C_{31}}$. (A) Biofilm formation and growth kinetics of the complementary strain CΔRpoA over 85 h. (B) Effect of $\mathbf{C_{31}}$ on bacterial growth within 24 h. (C and D) Inhibition of biofilm formation by $\mathbf{C_{31}}$. (E and F) Eradication of preformed biofilms by $\mathbf{C_{31}}$. (G) EPS production in the CΔRpoA strain and its suppression by $\mathbf{C_{31}}$. (H and I) Motility of the CΔRpoA strain and inhibition of bacterial movement by $\mathbf{C_{31}}$. (J and K) Pathogenicity of the CΔRpoA strain on rice and control efficacy of $\mathbf{C_{31}}$. (L) Hypersensitive response of CΔRpoA in tobacco and its suppression by $\mathbf{C_{31}}$. Data in (A), (B), (D), (F), (G), (I), and (K) are presented as mean ± SE. Significance was determined using an unpaired Student *t* test: $^*P < 0.05$, $^{**}P < 0.01$, $^{***}P < 0.001$, and $^{****}P < 0.0001$; ns, not significant ($n \geq 3$).

a minimal impact on bacterial growth (Fig. 4B) but significantly inhibited biofilm formation (Fig. 4C and D). At 2.0 × EC_{50}, $\mathbf{C_{31}}$ inhibited wild-type biofilm formation by 79.67%, which was significantly higher than that of TC (26.22%). At 4.0 × EC_{50} and 8.0 × EC_{50}, the inhibition rates reached 87.94% and 94.69%, respectively, both markedly superior to that of TC. High concentrations of $\mathbf{C_{31}}$ (8.0 × EC_{50}) also simultaneously suppressed bacterial proliferation. Additionally, ΔRpoA treated with $\mathbf{C_{31}}$ (2.0 × EC_{50}) showed no apparent changes in growth or biofilm formation, further indicating that RpoA deletion is the primary cause of the observed phenotypic defects and that $\mathbf{C_{31}}$ inhibits *Xoo* proliferation and biofilm formation by targeting RpoA.

In addition to inhibiting biofilm formation, $\mathbf{C_{31}}$ exhibited strong eradication capabilities against mature biofilms. Our observations indicated that *Xoo* biofilms tended to mature after 65 h of cultivation (Fig. 4A). Subsequently, we evaluated the efficacy of $\mathbf{C_{31}}$ and TC against mature biofilms. At 4.0 × EC_{50}, the eradication rates of mature biofilms by $\mathbf{C_{31}}$ and TC were 61.22% and 34.40%, respectively (Fig. 4E and F). When the concentration was increased to 16 × EC_{50}, the eradication rate of $\mathbf{C_{31}}$ increased substantially to 87.14%, whereas that of TC

reached only 42.04%. These data clearly demonstrated that to achieve a comparable level of biofilm disruption, TC requires a much higher concentration than $\mathbf{C_{31}}$. Therefore, although eradicating mature biofilms is inherently challenging and typically requires higher doses, $\mathbf{C_{31}}$ exhibits significantly superior efficacy compared to TC, confirming its potential as a highly effective biofilm-eradicating agent.

As a major component of the biofilm matrix, EPS provides physical protection and structural support to bacteria [29]. As shown in Fig. 4G, EPS production in ΔRpoA was significantly reduced, while CΔRpoA restored it to 88.87% of the wild-type level, consistent with the trend observed in biofilm formation. Both $\mathbf{C_{31}}$ and TC inhibited wild-type EPS production in a concentration-dependent manner, with $\mathbf{C_{31}}$ being more effective at reducing EPS production by 77.55% at 4.0 × EC_{50}. The impaired motility of ΔRpoA was also identified as one of the reasons for inhibited biofilm formation and pathogenicity. As indicated in Fig. 4H and I, the motility diffusion diameter of ΔRpoA was significantly reduced, while CΔRpoA restored motility to 89.38% of the wild-type level. The motility of the wild-type strain treated with $\mathbf{C_{31}}$ was significantly reduced (11.14 mm). In vivo rice experiments further confirmed (Fig. 4J and K) that both ΔRpoA and $\mathbf{C_{31}}$ treatment significantly reduced the pathogenicity of *Xoo*, while CΔRpoA restored approximately 81.05% of the susceptibility. The lesion length in the rice treated with $\mathbf{C_{31}}$ (3.54 cm) was significantly shorter than that in the TC-treated group (5.70 cm). Additionally, CΔRpoA restored the ability of the bacteria to induce an HR in tobacco, indicating that RpoA influences bacterial interaction with the host. Surprisingly, *N. benthamiana* treated with $\mathbf{C_{31}}$ (2.0 × EC_{50}) still developed necrotic spots similar to those induced by the wild-type strain (Fig. 4L). These observations are consistent with previous knockout experimental results, reinforcing the important contribution of RpoA to *Xoo* pathogenicity and virulence.

Compound $\mathbf{C_{31}}$ shows high binding affinity for RpoA

To validate the interaction between compound $\mathbf{C_{31}}$ and the key target, RpoA, we obtained a recombinant protein through prokaryotic expression (Fig. S6) and binding assays using the probe $\mathbf{C_{31}}$-$\mathbf{T_1}$ (Fig. 5A). The results showed that $\mathbf{C_{31}}$-$\mathbf{T_1}$ labeled *Xoo* RpoA in a dose-dependent manner, which was competitively inhibited by preincubation with excess $\mathbf{C_{31}}$. Pull-down assays further confirmed the specific binding between $\mathbf{C_{31}}$-$\mathbf{T_1}$ cells and RpoA, with no signal observed in the DMSO control, suggesting that *Xoo* RpoA is a direct target of $\mathbf{C_{31}}$.

To clarify the binding modes of $\mathbf{C_{31}}$ and $\mathbf{C_{31}}$-$\mathbf{T_1}$ to RpoA, we performed molecular docking based on the crystal structure of RpoA from *Xoo* PXO99A (PDB: 6J9E). The results demonstrated that both compounds bound to the same region of RpoA, forming hydrogen bonds with the key residues Ser175 and Arg180, as well as van der Waals interactions with Val179 (Fig. 5B and Fig. S7). In contrast, $\mathbf{C_{31}}$ exhibits a more extensive interaction network. In addition to the aforementioned hydrogen bonds, van der Waals forces were formed with Lys86, Asp87, and Val88 and engaged in alkyl/pi-alkyl interactions with Ala89, Tyr151, and Pro178. Taken together, these findings indicate that $\mathbf{C_{31}}$ possesses diverse interactions, consistent with its superior antibacterial activity.

We employed the Amber14SB force field (GROMACS) to simulate the binding of $\mathbf{C_{31}}$ and $\mathbf{C_{31}}$-$\mathbf{T_1}$ to RpoA. Root-mean-square deviation (RMSD) analysis revealed that both complexes remained stable during the 100-ns simulation (Fig. 5C), with the $\mathbf{C_{31}}$ complex exhibiting smaller overall fluctuations and greater conformational stability. Additionally, root-mean-square fluctuation (RMSF) analysis indicated minimal residue fluctuations (<0.11 nm, Fig. 5D), suggesting that binding did not disrupt the secondary structure of the protein. Analyses of the radius of gyration and solvent-accessible surface area (SASA) revealed that the complexes maintained their compact structures (Fig. 5E), with changes in solvent accessibility reflecting only local flexibility adjustments (Fig. 5F). Free energy landscape analysis showed that the conformational states of both $\mathbf{C_{31}}$–RpoA and $\mathbf{C_{31}}$-$\mathbf{T_1}$–RpoA complexes were confined to narrow, low-energy basins, indicating stable binding without inducing large-scale, drastic conformational changes in the protein. Notably, the energy well for the $\mathbf{C_{31}}$ complex was deeper and more confined than that for $\mathbf{C_{31}}$-$\mathbf{T_1}$, demonstrating that $\mathbf{C_{31}}$ formed a more thermodynamically stable complex and acted as a superior ligand (Fig. 5G and Fig. S8).

Dynamic trajectory analysis indicated that the RMSD of the RpoA–$\mathbf{C_{31}}$ complex was lower, with a narrower fluctuation range, than that of free RpoA. RMSF analysis also revealed a decrease in overall protein flexibility (Fig. 5H). SASA analysis further revealed reduced solvent accessibility in the direct binding region (A98-A113 and Y151), along with altered accessibility of distal functional residues (Fig. 5H). The secondary structure analysis indicated that the occupancy of α-helices and the content of β-sheets slightly increased throughout the simulation range (Fig. 5I and J), while the key functional segments (K86-I90, A98-A113, and Y151-R165) showed a substantial increase in the occupancy of β-bridges and a marked decrease in the occupancy of 3_{10} helices (Fig. S9). These results suggest that the binding of $\mathbf{C_{31}}$ maintains the overall stability of the protein while enhancing the local structural rigidity of key regions and restricting their conformational diversity, which is consistent with the mechanism by which $\mathbf{C_{31}}$ allosterically regulates protein function through the "molecular wedge" effect [30–32].

To quantitatively evaluate the binding between $\mathbf{C_{31}}$ and RpoA, the binding response was assessed using biolayer interferometry (BLI). Weak responses (<0.10 nm) were observed for low-activity compounds ($\mathbf{C_7}$, $\mathbf{C_8}$, $\mathbf{C_9}$, $\mathbf{C_{10}}$, and $\mathbf{C_{11}}$), whereas the highly active compound $\mathbf{C_{31}}$ (>0.18 nm) exhibited a strong response (Fig. 5K). Although not all compounds showed a strong positive correlation between activity and response value, structural modifications such as the introduction of a benzyl group and extension of the bridging chain markedly enhanced the binding affinity. $\mathbf{C_{31}}$ demonstrated the highest affinity for RpoA (dissociation constant [K_D] = 1.61 μM, Fig. 5L), which was 8.24-fold stronger than that of the bactericide TC (K_D = 13.26 μM, Fig. 5M). Microscale thermophoresis (MST) experiments further confirmed the high affinity of $\mathbf{C_{31}}$ (K_D = 0.56 μM), which was 35.89-fold greater than that of TC (K_D = 20.10 μM, Fig. 5N). Collectively, these computational and experimental results suggest that compound $\mathbf{C_{31}}$ binds favorably to RpoA, further supporting that RpoA is a molecular receptor for $\mathbf{C_{31}}$.

$\mathbf{C_{31}}$ targets *Xoo* RpoA and inhibits its LLPS-driven condensate formation

In bacteria, biomacromolecules such as proteins and nucleic acids undergo LLPS to form membraneless organelles, a process that plays a key role in cellular organization and functional regulation [4]. Taking *E. coli* RpoA as an example, although the N-terminal domain (αNTD) and C-terminal domain (αCTD)

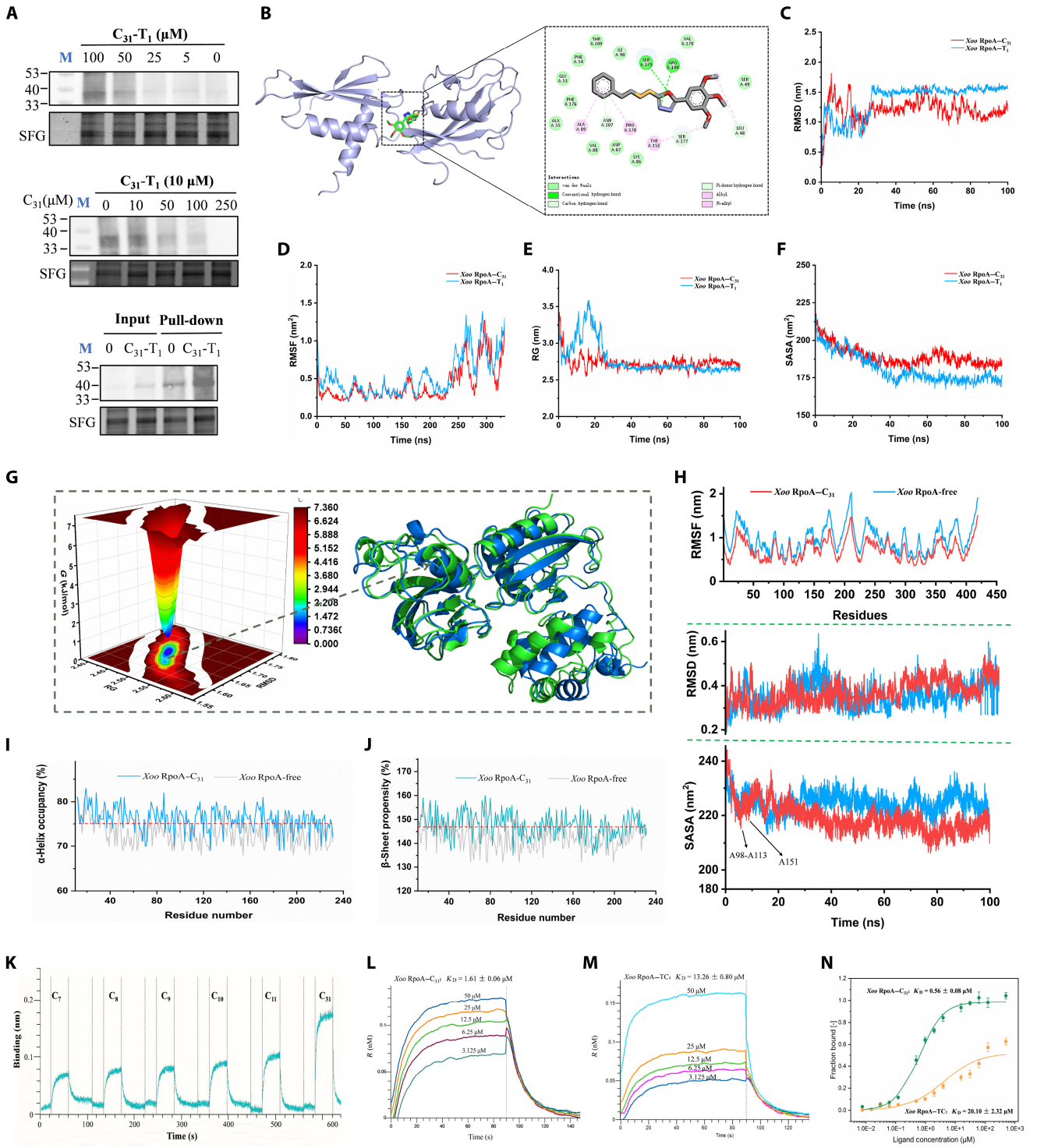


Fig. 5. Direct interaction between **C_{31}** and *Xoo* alpha subunit of RNA polymerase (RpoA). (A) Dose-dependent labeling of *Xoo* RpoA by **C_{31}-T_1** in *Xoo* lysates, competitively inhibited by unmodified **C_{31}**. No labeling in the dimethyl sulfoxide (DMSO) control. Western blot with anti-RpoA antibody confirms protein identity; SFG shows equal loading. (B) The 3-dimensional (3D) and 2-dimensional (2D) binding models of compound **C_{31}** at the active site of *Xoo* RpoA. (C to F) Molecular dynamics simulations of *Xoo* RpoA with **C_{31}** or **C_{31}-T_1**, showing root-mean-square deviation (RMSD), root-mean-square fluctuation (RMSF), radius of gyration (RG), and solvent-accessible surface area (SASA). (G) Free energy landscape (FEL) and representative conformations of the *Xoo* RpoA–**C_{31}** complex. (H to J) Molecular dynamics (MD) simulations of RpoA with or without **C_{31}**, showing stability, flexibility, and secondary structure. (K) Biolayer interferometry (BLI) sensorgrams showing the binding response of various active compounds (10 μM) to immobilized *Xoo* RpoA. (L and M) BLI-based binding curves and fitting for **C_{31}** and TC (concentration range: 3.125 to 50 μM). (N) Binding curves and dissociation constants for **C_{31}** and TC with *Xoo* RpoA, as determined using microscale thermophoresis (MST) (concentration range: 0.01 to 1,000 μM).

are predominantly structured regions, they still contain short intrinsically disordered regions. The proline-rich region between Pro-10 and Pro-20 in αNTD can mediate phase separation through multivalent, dynamic weak interactions [33]. Based on this conserved feature, we used IUPred2A to predict the disorder propensity of the *Xoo* RpoA protein sequence and assess its potential for phase separation [34]. This tool integrates the IUPred2 energy estimates for ordered/disordered residues with ANCHOR2 predictions for disordered binding regions. Comprehensive analysis indicated the presence of partially disordered regions within the *Xoo* RpoA domain (Fig. S10). This result suggests that RpoA may possess a molecular basis for phase separation.

To experimentally validate whether *Xoo* RpoA undergoes phase separation, we transiently expressed the RpoA–green fluorescent protein (GFP) fusion protein in *N. benthamiana* leaves (Fig. S11 and Fig. 6A and B). Distinct fluorescent condensates were observed at 24 h postexpression. By 32 h, the number of condensates had significantly increased, and at 40 h, these granules coarsened, manifesting as larger sizes and reduced numbers. To further investigate the inhibitory effect of compound $\mathbf{C_{31}}$ on condensate formation, we injected $\mathbf{C_{31}}$ (at a concentration of $16 \times EC_{50}$) or DMSO (solvent control) into the left side of the same leaf region at 24 h postexpression and monitored the dynamics of the IBs via Z-stack scanning at 8 and 16 h postinjection. Compared with the DMSO group, $\mathbf{C_{31}}$ treatment significantly reduced the number of small IBs and their diffuse distribution within cells at 32 h. By 40 h, the number of IBs was reduced by 61.92% (*t* test, $P < 0.0001$; Fig. 6C). In contrast, the commercial bactericide TC reduced the number of aggregates by only 29.65% (*t* test, $P = 0.0002$; Fig. S12). This trend aligns with their antibacterial activities, indicating that $\mathbf{C_{31}}$ effectively inhibits RpoA-dependent condensate formation.

Furthermore, time-lapse confocal imaging revealed that small, dynamic IBs fused and gradually coalesced into larger particles (Fig. 6D and Video S1), whereas larger condensates underwent fission after 32 h, generating small particles that redispersed and relaxed into spherical structures (Fig. 6E and Video S2). These dynamic behaviors, including motility, fusion, fission, and spherical morphology, collectively suggest that IBs formed by *Xoo* RpoA exhibit liquid-like properties. To quantitatively assess the dynamics of the condensates, we performed fluorescence recovery after photobleaching (FRAP) assays. The results showed that the fluorescence intensity of the photobleached condensates decreased to below 50% and subsequently recovered over time (Fig. 6F and G), indicating continuous molecular exchange and high fluidity within the condensates. To further examine the LLPS properties of these condensates, they were treated with 1,6-hexanediol and PEG 8000. At 32 h postinjection, 1,6-hexanediol treatment substantially reduced the condensate numbers, whereas PEG 8000 enhanced both condensate abundance and size (Fig. 6H). Overall, these findings clearly demonstrate that *Xoo* RpoA can form BMCs with LLPS characteristics, and $\mathbf{C_{31}}$ may behave as the inhibitor of such a process.

The above computational analysis (Fig. 5B and H to J and Fig. S9) suggests that $\mathbf{C_{31}}$ may interfere with the interaction between RpoA and key factors such as σ^{70} by binding to and allosterically modulating the C-terminal domain of RpoA. To elucidate the nature of the phase-separation process inhibited by $\mathbf{C_{31}}$, we sought to determine whether the phenomenon represents a single-component behavior of RpoA or a multicomponent co-condensation driven by its interaction with essential partners such as σ^{70}. Given that σ^{70} serves as a core component of RNA polymerase (RNAP) and a master regulator of global transcription [35–37], we first focused on examining the role of RpoA–σ^{70} interaction in phase separation. To this end, we expressed and purified enhanced green fluorescent protein (EGFP)–RpoA and EGFP–σ^{70} in vitro (Fig. S13) and examined their phase-separation behaviors individually and in combination under defined buffer conditions. Confocal microscopy revealed that neither protein alone formed discernible condensates (Fig. 6I). However, when mixed at equimolar concentrations (10 μM each), they readily formed small condensates. The addition of PEG 8000 promoted condensate formation and growth in a concentration-dependent manner (Fig. 6J). FRAP analysis revealed rapid fluorescence recovery within these condensates, indicating the active molecular exchange and liquid-like dynamic characteristics of LLPS (Fig. 6K and L). To validate this interaction in living cells, we constructed an mScarlet–σ^{70} expression vector and transiently expressed it in *N. benthamiana* leaves. When expressed alone, mScarlet–σ^{70} displayed diffuse cytoplasmic distribution. In contrast, coexpression with RpoA–GFP led to the formation of prominent condensates, with clear signal colocalization in a subset of these structures, confirming specific recruitment of σ^{70} into RpoA condensates (Fig. 6M and N). These findings suggest that *Xoo* RpoA drives co-condensate assembly through recruitment of the core sigma factor σ^{70}.

RpoA globally regulates the high-level expression of virulence-associated factors in *Xoo*

To elucidate the function of RpoA, we conducted transcriptome sequencing analysis of the wild-type PXO99^{A} and its ΔRpoA mutant. A total of 4,304 coexpressed genes were detected (Fig. 7A), among which 407 were identified as significantly differentially expressed genes (DEGs) (Fig. 7B), including 224 up-regulated and 183 down-regulated genes ($|\log_2 FC| \geq 1$). Gene Ontology enrichment analysis revealed that the DEGs were primarily associated with cellular anatomical entities, the plasma membrane, and the cell periphery in the cellular component category; involved in the regulation of molecular function, regulation of catalytic activity, and biosynthetic processes in the biological process category; and enriched in catalytic activity, binding, transferase activity, and small-molecule binding in the molecular function category (Fig. 7C and Supplementary Materials II). Kyoto Encyclopedia of Genes and Genomes pathway analysis indicated that the DEGs were significantly enriched in pathways such as the 2-component system, oxidative phosphorylation, and bacterial secretion system, with predominantly down-regulated genes. This suggests that RpoA plays a crucial role in facilitating high-level transcription of a global virulence program (Fig. 7D and Supplementary Materials II).

To further validate the regulatory effects of RpoA, RT-qPCR was performed to analyze changes in the expression of key genes in multiple pathways after treating the wild-type strain with compound $\mathbf{C_{31}}$. The results showed that $\mathbf{C_{31}}$ significantly suppressed the expression of exopolysaccharide synthesis genes *gumB*, *gumC*, *gumH*, and *gumN* (down-regulated by 51.04% to 68.15%), indicating that it inhibits EPS production by repressing the *gum* gene cluster without affecting bacterial growth (Fig. 7E). Genes associated with motility and chemotaxis, including *flgB*, *fliA*, *cheR*, and *cheW*, were also significantly down-regulated (35.35% to 51.74%), demonstrating that $\mathbf{C_{31}}$ inhibits bacterial movement and chemotactic behavior, thereby indirectly impairing biofilm formation (Fig. 7F). Similarly, genes related to the

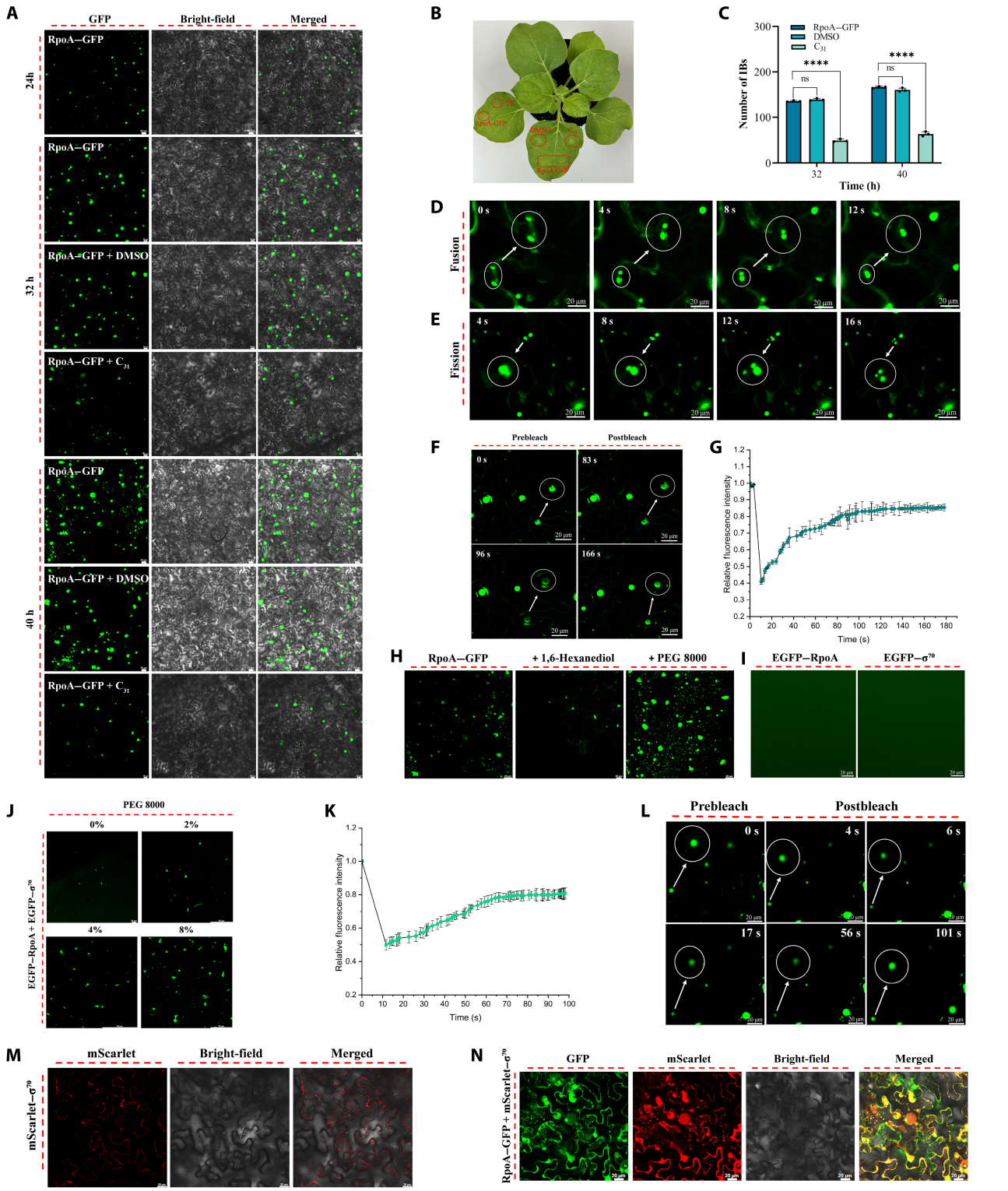


Fig. 6. Compound $\mathbf{C_{31}}$ suppresses the phase separation and dynamics of *Xoo* RpoA condensates in planta. (A and B) Fluorescence images showing that $\mathbf{C_{31}}$ treatment reduces the formation of *Xoo* RpoA inclusion bodies (IBs) in *Nicotiana benthamiana* leaves compared to the DMSO control. (C) Quantification of IBs at 32 and 40 h; data are presented as individual values with mean ± SD ($n = 4$); ***$P < 0.001$ (2-sided t test, $P = 0.0001$). (D and E) Time-lapse images showing IB fusion and fission at 32 h. White circles indicate fusing or fissioning IBs. (F and G) Fluorescence recovery after photobleaching (FRAP) analysis of IBs showing fluorescence recovery kinetics. Data are presented as mean ± SD. (H) Effects of 10% 1,6-hexanediol and PEG 8000 on IB formation. (I) Enhanced green fluorescent protein (EGFP)–RpoA or EGFP–σ^{70} alone does not form condensates. (J) Condensate formation after mixing purified EGFP–RpoA and EGFP–σ^{70} (10 μl each) in buffer with increasing concentrations of PEG 8000. (K and L) FRAP analysis of in vitro droplets formed by EGFP–RpoA and EGFP–σ70. (M and N) Colocalization of RpoA–green fluorescent protein (GFP) and mScarlet–σ^{70} in condensates. Scale bars, 20 μm (A, D, E, F, H to J, and L to N).

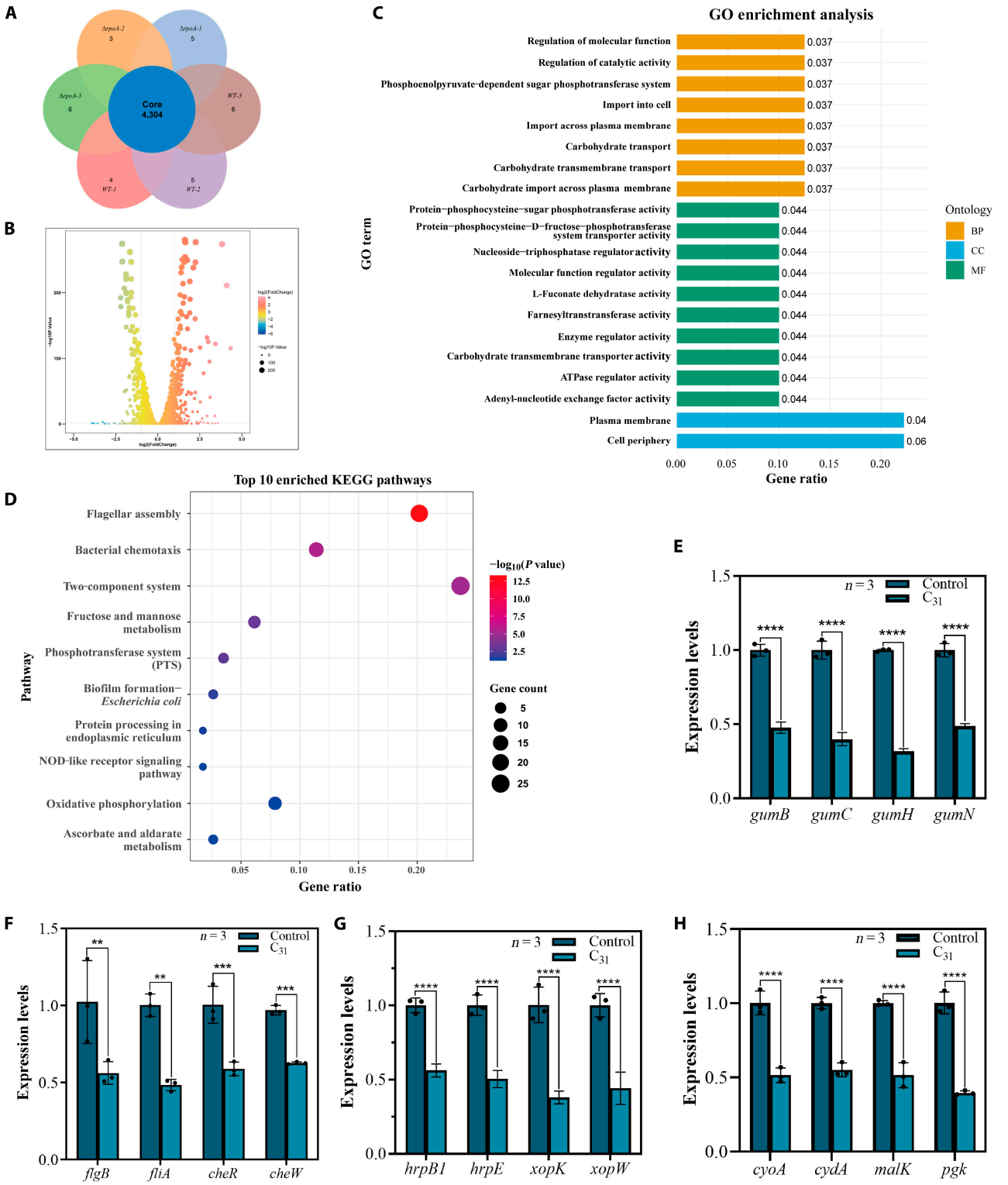


Fig. 7. Transcriptomic profiling of the ΔRpoA mutant and **C_{31}**-mediated suppression of virulence genes. (A) Venn diagram illustrating the overlap of expressed genes in the WT and ΔRpoA strains. (B) Volcano plot of differentially expressed genes (DEGs) between the WT and ΔRpoA strains. (C) Gene Ontology (GO) enrichment analysis of DEGs across the biological process (BP), molecular function (MF), and cellular component (CC) categories. (D) Kyoto Encyclopedia of Genes and Genomes (KEGG) pathway enrichment analysis of DEGs. (E to H) Relative expression levels of key virulence genes in *Xoo* treated with **C_{31}** ($2 \times EC_{50}$), quantified using reverse transcription quantitative polymerase chain reaction (RT-qPCR): (E) exopolysaccharide (gum) biosynthesis genes, (F) motility and chemotaxis genes, (G) energy metabolism genes, and (H) type III secretion system genes. Data in (E) to (H) are presented as mean ± SE. Significance was determined using an unpaired Student *t* test: $^{*}P < 0.05$, $^{**}P < 0.01$, $^{***}P < 0.001$, and $^{****}P < 0.000$; ns, not significant ($n \geq 3$).

type III secretion system, such as *hrpB1*, *hrpE*, *xopK*, and *xopW*, were notably down-regulated (43.88% to 62.16%), suggesting a potential attenuation of bacterial pathogenicity (Fig. 7G). Furthermore, energy metabolism genes, including *cyoA*, *cydA*, *malK*, and *pgk*, exhibited widespread decreased expression (44.96% to 60.52%), reflecting the broad inhibitory effect of $\mathbf{C_{31}}$ on the bacterial energy supply system (Fig. 7H). These transcriptome profiles suggest that RpoA deletion or $\mathbf{C_{31}}$ treatment disrupts multiple pathogenicity-associated pathways in *Xoo*, primarily through transcriptional down-regulation.

RpoA is evolutionarily conserved in *Xanthomonas*, and pathogens exhibit low propensity for developing resistance to $\mathbf{C_{31}}$

Considering that green pesticides should demonstrate broad-spectrum efficacy against pests while ensuring safety for nontarget organisms [38], we performed phylogenetic and conservation analyses of *Xoo* RpoA. The results revealed that RpoA was a highly conserved target within the *Xanthomonas* genus (Fig. 8A). This conservation is evident in the phylogenetic relationships consistent with species evolution and, more importantly, in the near-perfect sequence conservation of its N-terminal assembly domain, particularly in the regions critical for maintaining core functions (Fig. 8B). This finding is of particular interest. Given the high homology of the $\mathbf{C_{31}}$ target RpoA in *X. oryzae* pv. *oryzicola* (*Xoc*) and *X. axonopodis* pv. *citri* (*Xac*) and identical sequences of their key functional regions, we investigated the broad-spectrum antibacterial potential of $\mathbf{C_{31}}$ and evaluated its control efficacy against bacterial leaf streaks of rice (caused by *Xoc*) and citrus bacterial cankers (caused by *Xac*). Prior to conducting in vivo experiments, we assessed the antibacterial activity of $\mathbf{C_{31}}$ against *Xoc* and *Xac*. $\mathbf{C_{31}}$ exhibited the strongest antibacterial activity against both *Xoc* and *Xac* (Table S3, with EC_{50} values of 1.99 and 2.31 μg/ml, respectively), leading us to anticipate that it would also demonstrate efficacy in plants. As shown in Fig. 8C, the average lesion lengths in the control and SA-treated groups were 48.56 and 29.50 mm, respectively, while treatment with the same concentration of $\mathbf{C_{31}}$ resulted in a lesion length of only 13.57 mm, with a control efficacy of 71.98%, significantly higher than those of SA (38.98%) and TC (59.70%). Moreover, the control leaves exhibited numerous typical cancer lesions, while treatment with 200 μg/ml $\mathbf{C_{31}}$ significantly mitigated disease symptoms (Fig. 8D), with a preventive effect of 64.23%, far superior to those of SA (25.09%) and TC (51.24%).

To investigate the crop safety of compound $\mathbf{C_{31}}$, we sprayed rice and citrus leaves with a high concentration of 500 μg/ml $\mathbf{C_{31}}$ solution. After 7 d, the plants grew normally without any phytotoxicity or morphological abnormalities (Fig. 8E), indicating that the compound was safe for rice and citrus, even at doses far exceeding the effective concentration. Additionally, to evaluate the sustained efficacy of $\mathbf{C_{31}}$, *Xoo* bacterial suspension was inoculated on the 1st, 3rd, 7th, and 10th days after spraying 200 μg/ml $\mathbf{C_{31}}$, and the control efficacy was investigated 14 d later. As shown in Fig. S14, $\mathbf{C_{31}}$ exhibited good persistence, maintaining a control efficacy of 47.19% to 61.56% even when inoculated on the 10th day, significantly superior to that of TC (32.24% to 53.69%). This indicates that $\mathbf{C_{31}}$ has the potential to sustain the control of bacterial diseases in field applications.

To evaluate the potential development of bacterial resistance to $\mathbf{C_{31}}$, wild-type $PXO99^{A}$ was induced for 1 to 12 generations with 0.86 μg/ml (1 × EC_{50}) of $\mathbf{C_{31}}$, and the EC_{50} value for each generation was determined. As shown in Fig. S15, the EC_{50} values of the $\mathbf{C_{31}}$-treated group remained stable (0.88 to 0.99 μg/ml), increasing only 1.12-fold after 12 generations. In contrast, the EC_{50} values of the TC-treated group gradually increased from the second generation onward (64.49 to 106.41 μg/ml), ultimately rising 1.64-fold. These results indicate that under experimental conditions, *Xoo* is unlikely to develop resistance to $\mathbf{C_{31}}$ easily.

Discussion

In the pursuit of novel bactericidal lead structures, we employed a molecular hybridization strategy conjugating a naturally derived SA scaffold (recognized for its antimicrobial potential) with a disulfide-bearing 1,3,4-oxadiazole moiety. This approach afforded a series of hybrid molecules, $\mathbf{C_1}$ to $\mathbf{C_{34}}$ (Fig. 1A). The synthesis was efficiently accomplished in 3 straightforward steps using commercially available starting materials (Fig. S1). Furthermore, the inherent phenolic hydroxyl and carboxylic acid functional groups within the SA scaffold provided advantageous sites for structural derivatization. Bioactivity evaluation revealed that derivative $\mathbf{C_{31}}$ exhibited exceptional inhibitory activity against *Xoo*, with an EC_{50} value of 0.86 μg/ml (Table 1). In subsequent in vivo pot experiments, $\mathbf{C_{31}}$ demonstrated a control efficacy of 59.37% against *Xoo*-induced rice BLB, significantly outperforming both the parent compound SA and commercial bactericide TC (Fig. 1D and E).

To elucidate the molecular receptor of $\mathbf{C_{31}}$ within *Xoo*, we used ABPP, which identified 3 potential protein targets: RpoA, Tsf, and DsbA (Fig. 2). We successfully constructed knockout mutants for the genes encoding these proteins (ΔRpoA, ΔTsf, and ΔDsbA) and compared their impacts on *Xoo* pathogenicity and virulence. The ΔRpoA mutant displayed a profound pathogenic defect, with virulence reduced by 87.4%, and completely lost the ability to elicit an HR in tobacco (Fig. 3B to D). Furthermore, this mutant exhibited severe impairment in biofilm formation, EPS production, motility, and growth capacity. In contrast, mutants of the other candidate genes (ΔTsf and ΔDsbA) showed only minor phenotypic alterations (Fig. 3E to K). The construction of a genetically complemented strain, CΔRpoA (Fig. S5), resulted in the marked restoration of virulence-associated physiological, biochemical, and pathogenic traits to levels comparable to those of the wild-type strain (Fig. 4). These findings unequivocally underscore the critical contribution of RpoA to *Xoo* pathogenicity. Direct binding assays confirmed that $\mathbf{C_{31}}$ interacts with recombinant RpoA protein with high affinity, exhibiting a K_D value in the range of 0.56 to 1.61 μM (Fig. 5L and N). Molecular docking revealed that $\mathbf{C_{31}}$ interacted with the key residues Ser175, Arg180, and Val179 of RpoA (Fig. 5B). Dynamic simulations further confirmed that a stable complex was formed between $\mathbf{C_{31}}$ and RpoA (Fig. 5C to G). Although the binding of $\mathbf{C_{31}}$ did not disrupt the secondary structure of the protein, it substantially restricted the conformational diversity of the key interface region of RpoA by inducing local β-sheet formation and reducing the accessibility of key interface residues (Fig. 5H to J and Fig. S9). These results confirm that RpoA is a functional in vivo receptor of $\mathbf{C_{31}}$ in *Xoo*.

In eukaryotes, the formation of BMCs by RNAPs via LLPS is an important transcriptional regulatory mechanism. For example, a study [39] confirmed that RNAP I can form condensates and participate in transcriptional repression of ribosomal DNA. Although direct observation of RpoA phase separation has not yet been reported in *Xoo*, the formation of LLPS condensates by

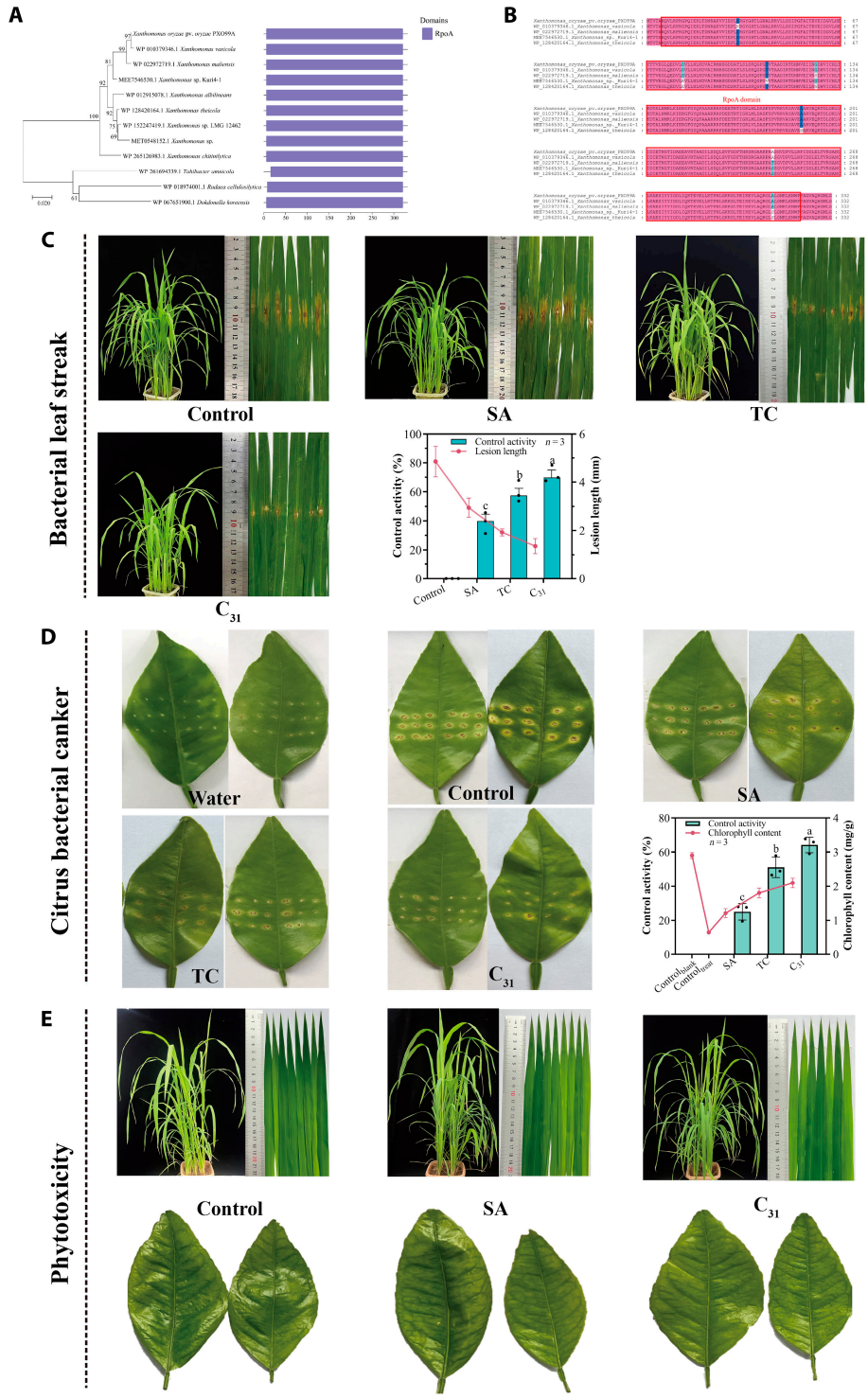


Fig. 8. RpoA conservation and broad-spectrum efficacy of $\mathbf{C_{31}}$ against *Xanthomonas*. (A) Phylogenetic analysis and domain architecture of RpoA across *Xanthomonas* strains, illustrating its conserved 2-domain structure. (B) Multiple sequence alignment of the RpoA N-terminal domain, highlighting identical key functional residues (red) among *Xoo*, *X. oryzae* pv. *oryzicola* (*Xoc*), and *X. axonopodis* pv. *citri* (*Xac*). (C) In vivo control efficacy of $\mathbf{C_{31}}$ (200 μg/ml) against bacterial leaf streak (BLS) caused by *Xoc*, compared with TC and SA. Lesion lengths were measured at 14 d postinoculation. (D) In vivo protective efficacy of $\mathbf{C_{31}}$ (200 μg/ml) against citrus bacterial canker (CBC) caused by *Xac*, compared with TC and SA. Disease severity was assessed at 14 d postinoculation. (E) Phytotoxicity assessment of $\mathbf{C_{31}}$ (500 μg/ml) on rice and citrus plants at 7 d posttreatment, showing no visible damage. Data in (C) and (D) are presented as mean ± SE. Different lowercase letters indicate statistically significant differences (one-way ANOVA with LSD post hoc test, $P < 0.05$; $n \geq 3$).

RNAP in prokaryotes, such as *E. coli* and *Bacillus subtilis*, has been documented in multiple studies [40,41], providing indirect evidence for the existence of a similar mechanism in *Xoo*. Through bioinformatics analysis, we predicted that the *Xoo* RpoA protein contains intrinsically disordered regions, suggesting its potential to undergo LLPS (Fig. S10). To validate this

hypothesis, we transiently expressed *Xoo* RpoA in plant cells and successfully observed the formation of BMCs. Treatment with compound $\mathbf{C_{31}}$ significantly reduced the number of these condensates (Fig. 6A to C). Further dynamic observations revealed that during the early stages of condensate formation, multiple small condensates collided and fused into larger droplets (Fig. 6D and E), indicating typical liquid-like behavior. To quantitatively characterize the fluid properties, we employed FRAP to assess protein mobility within the condensates. The results showed that fluorescence in the bleached area gradually recovered over time (Fig. 6F and G), demonstrating the free diffusion of protein molecules within the condensates and further confirming their liquid nature.

The bacterial RpoA not only contributes to RNAP holoenzyme assembly but also functions as a major integration hub for transcription regulation. Through its C-terminal domain (αCTD), RpoA contacts upstream promoter DNA elements and diverse transcription activators, thereby coupling upstream regulatory inputs to σ^{70}-dependent promoter recognition and the formation of transcriptionally competent open complexes [36]. Importantly, functional interactions between αCTD and σ^{70} region 4 have been demonstrated to bridge upstream elements/activators with core promoter recognition, providing a mechanistic basis by which αCTD can facilitate both RNAP recruitment and remodeling of RNAP–promoter interactions to enhance initiation at specific promoters [37]. σ^{70} associates reversibly with core RNAP and can be replaced by alternative σ factors [35]; competition among σ factors for a limited pool of core RNAP contributes to coordinated expression of gene sets underlying distinct physiological functions. Consistent with the importance of σ^{70}-dependent transcription in plant pathogenicity, recent work in *Xoo* demonstrated that the σ^{70} factor directly binds the promoter of *PXO_trpR* to control motility and oxidative-stress tolerance and also directly binds the *hrpG* and *hrpX* promoters to modulate T3SS gene expression and effector deployment [42,43]. These imply that for virulence genes predominantly driven by σ^{70}, transcriptional amplitude, induction thresholds, and responsiveness to upstream activators can, in principle, be modulated by the RpoA–σ^{70} interaction interface and the recruitment/remodeling capacity of αCTD. Notably, we found that purified RpoA alone did not form condensates in vitro, whereas droplets formation was observed upon addition of σ^{70} (Fig. 6I to N), suggesting that reversible RpoA–σ^{70} association may promote LLPS-like assembly of membraneless transcriptional hubs. This interpretation is consistent with recent evidence that bacterial RNAP can form dynamic clusters with properties attributable to LLPS [44].

Given that BMCs can be selectively permeable, we speculate that RNAP clustering during infection could, in principle, bias the partitioning of σ factors and thereby contribute to fine-tuning of alternative σ programs [33,45]. Transcriptome analysis of the ΔRpoA mutant supported this hypothesis (Fig. 7E to H), revealing a broad disruption of σ^{70}-mediated transcription and significant down-regulation of genes governing biofilm synthesis, motility, and the type III secretion system. The detailed downstream effects on specialized regulons (e.g., those controlled by σ^{54} and σ^{28}) were likely attributable to the primary disruption of this core transcriptional infrastructure. Thus, inside bacterial cells, RpoA engages σ^{70} through a reversible interaction involving the αCTD, creating multivalent contacts that can promote LLPS. This leads to the assembly of a membraneless RpoA–σ^{70} condensate, within which RpoA/σ^{70} complexes are enriched together with DNA templates, thereby increasing the local concentration of initiation components and facilitating robust σ^{70}-dependent transcription. Conversely, compound $\mathbf{C_{31}}$ is shown to bind at the RpoA–σ^{70} interface, impairing their association and blocking condensate formation. Similarly, genetic loss of RpoA prevents productive RpoA–σ^{70} coupling. Both perturbations disrupt the LLPS-enabled transcriptional hub, destabilize global transcriptional homeostasis, and ultimately attenuate bacterial virulence (Fig. 9).

In summary, the study revealed that targeting the core transcriptional regulatory subunit RpoA of *Xoo* and its phase-separation behavior represented a highly promising novel antibacterial strategy. We found that RpoA undergoes LLPS within host cells to form BMCs, and this process may depend on its specific interaction with the primary sigma factor σ^{70}. Based on these findings, we proposed a model in which the RpoA–σ^{70} phase-separation interface may constitute a novel regulatory mechanism that organizes virulence transcriptional programs through biophysical phase transitions. The ΔRpoA mutation severely impaired bacterial virulence and associated phenotypes, and transcriptomic analysis further indicated that this disruption stems from dysregulation of the σ^{70}-governed global virulence network, thereby supporting the proposed mechanism. Compound $\mathbf{C_{31}}$ effectively inhibited the phase-separation capacity of RpoA and disrupted the RpoA–σ^{70} interaction interface via allosteric interference, dismantling this transcriptional hub at both physical and functional levels and thus strongly suppressing bacterial pathogenicity. Given the high conservation of RpoA across the *Xanthomonas* genus, $\mathbf{C_{31}}$ also exhibited excellent control efficacy against *Xoc* and *Xac*, with a low propensity to induce drug resistance. Overall, this study not only provides the lead compound $\mathbf{C_{31}}$ for controlling plant bacterial diseases but also offers novel mechanistic insights into interfering with pathogen virulence programs from the perspective of "phase separation–regulated transcription".

Materials and Methods

Materials and bacterial strain source

The reagents used in this study were sourced from commercial suppliers. The standard strain PXO99^{A} of *Xoo* was generously provided by Professor Fengquan Liu of Nanjing Agricultural University, Nanjing, China.

Synthesis and characterization of target compounds $\mathbf{C_1}$ to $\mathbf{C_{34}}$

The starting material, SA, was converted into key intermediate **2**, which contained a functionalized 1,3,4-oxadiazole moiety, through sequential esterification, substitution, hydrazinolysis, and cyclization. Subsequently, intermediate **2** was reacted with DDQ and various substituted thiols to yield 34 target compounds $\mathbf{C_1}$ to $\mathbf{C_{34}}$. Detailed synthetic procedures and structural characterization data are provided in Supplementary Materials I.

Construction of knockout and complementation strains for the target genes

Mutant strains were generated following a reported method [46] with slight modifications, as illustrated by the construction of the *RpoA* gene deletion mutant (ΔRpoA) and its complementary strain (CΔRpoA). The ΔRpoA mutant was generated via

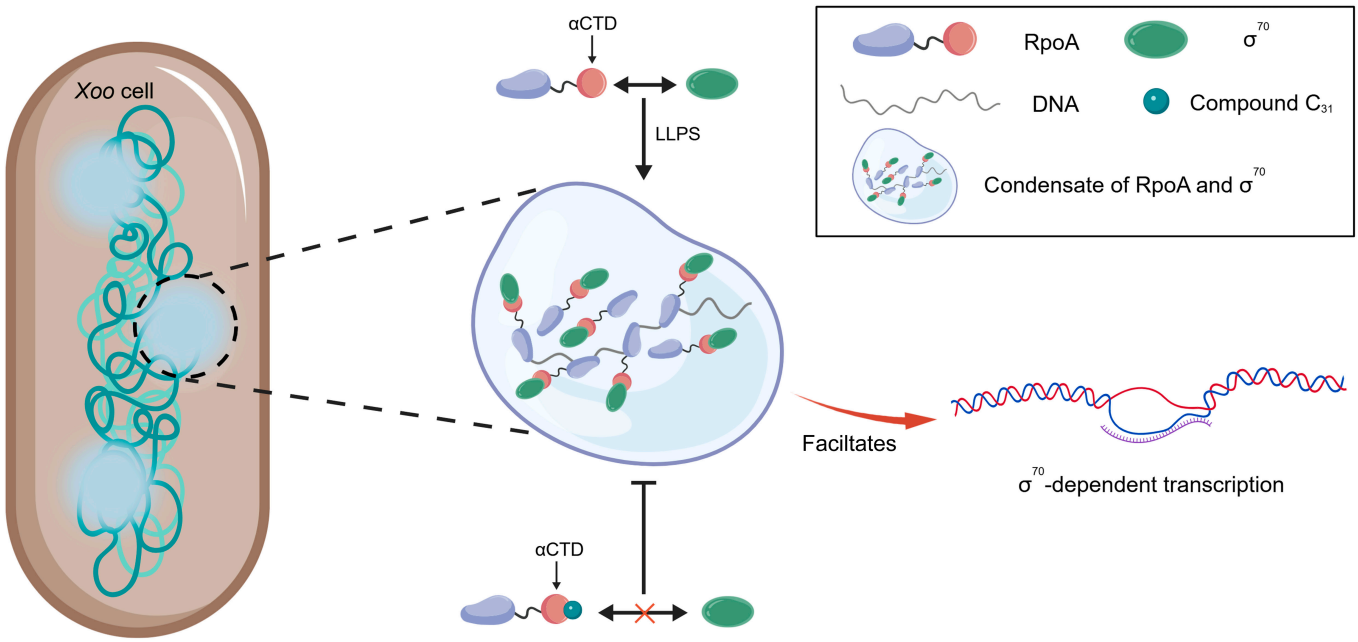


Fig. 9. Proposed model of RpoA–σ^{70}-driven condensate formation and transcriptional control. RpoA reversibly interacts with σ^{70} via the C-terminal domain (αCTD), promoting LLPS and the formation of a membraneless RpoA–σ^{70} condensate. The condensate enriches RpoA/σ^{70} complexes and DNA, thereby facilitating efficient σ^{70}-dependent transcription. Small molecule $\mathbf{C_{31}}$ is proposed to disrupt the RpoA–σ^{70} interface, preventing condensate assembly and leading to transcriptional dysregulation and reduced pathogenicity. This figure was created with biogdp.com [51].

homologous recombination using the suicide vector pK18mobsacB. Briefly, the upstream and downstream homologous arms of the *RpoA* gene were amplified from PXO99^{A} genomic DNA and ligated into pK18mobsacB. The resulting knockout plasmid was electroporated into PXO99^{A} competent cells. Positive recombinants were selected using a 2-step process on plates containing kanamycin and sucrose. The complementary strain CΔRpoA was constructed by cloning the *RpoA* gene into the pBBR1MCS-5 vector (conferring gentamicin resistance), followed by selection on gentamicin-containing plates. All constructed strains were verified using PCR and DNA sequencing.

Biofilm formation assay

Wild-type PXO99^{A}, knockout mutant, and complementary strains were grown in nutrient broth (NB) to the logarithmic phase (OD_{595} = 0.6 to 0.8). Bacterial cells were collected via centrifugation, resuspended in sterile water, and adjusted to an OD_{595} = 0.2. Aliquots (200 μl) of each suspension were transferred into 96-well plates. The wild-type PXO99^{A} suspensions were treated with serial concentrations of $\mathbf{C_{31}}$ or TC (0–16 × EC_{50}; 0.5% DMSO as control), whereas the ΔRpoA mutant suspension was treated with $\mathbf{C_{31}}$ at 2 × EC_{50}. After 85 h of static incubation at 28 °C, the medium was carefully removed, and nonadherent cells were washed away with water. Adherent biofilms were stained with 0.1% crystal violet, washed, air-dried, and solubilized in 95% ethanol. The absorbance at 570 nm was measured to quantify the biofilm biomass.

Assessment of preformed biofilm disruption

Biofilms were established by culturing the wild-type PXO99^{A} strain in 96-well plates for 75 h at 28 °C. After 2 washes with phosphate-buffered saline, the preformed biofilms were treated with various concentrations of $\mathbf{C_{31}}$ or TC in the NB medium and incubated overnight. Subsequently, the treatment solutions were aspirated, and any remaining planktonic cells were removed by washing with phosphate-buffered saline. The remaining adherent biofilms were quantified by staining with 0.1% crystal violet for 30 min. After rinsing and air-drying, the bound dye was dissolved in 95% ethanol, and the absorbance was measured at 570 nm.

Quantification of EPS

Bacterial suspensions of the wild-type PXO99^{A}, knockout mutant, and complementary strains were adjusted to OD_{595} = 0.2 and spotted on nutrient agar (NA) plates. Following incubation at 28 °C for 48 h, the plates were incubated at room temperature for an additional 72 h for observation of colony morphology and color. For EPS extraction, 200 μl of an overnight bacterial culture was inoculated into 20 ml of NB medium. The wild-type PXO99^{A} culture was treated with a concentration gradient of $\mathbf{C_{31}}$ or TC (0.5–8.0 × EC_{50}) and incubated with shaking (180 rpm) at 28 °C for 72 h. The EPS was precipitated from the cell-free supernatant by adding 3 volumes of 95% ethanol and storing at 4 °C overnight. The precipitate was collected by centrifugation, dried, and weighed to determine the EPS content. All experiments included 3 independent biological replicates.

Swimming motility assay

Bacterial suspensions of wild-type PXO99^{A}, knockout mutants, and complementary strains were adjusted to an OD_{595} = 0.2. Aliquots (2 μl) of each suspension were spotted onto semisolid NA (0.6% agar) plates. For chemical treatment, wild-type PXO99^{A} was preincubated with $\mathbf{C_{31}}$ or TC (2.0 × EC_{50}) for 12 h prior to spotting, with 0.5% DMSO serving as a vehicle control. All plates were incubated at 28 °C for 72 h, and the migration diameters of the colonies were measured.

Growth kinetics assay

The growth rates of the wild-type PXO99^A, knockout mutants, and complementary strains were assessed. Bacterial suspensions (OD_{595} = 0.2) were inoculated into NB medium. The wild-type strain was treated with a concentration gradient of $\mathbf{C_{31}}$ or TC (0–8.0 × EC_{50}), whereas the ΔRpoA mutant was treated with $\mathbf{C_{31}}$ at 2.0 × EC_{50}; 0.5% DMSO served as the vehicle control. All cultures were shaken (180 rpm) at 28 °C for 90 h, and bacterial growth was monitored by measuring the OD_{595} every 5 h.

Pathogenicity assay

Pathogenicity was evaluated in rice plants at the tillering stage [47]. Bacterial suspensions of wild-type PXO99^A, knockout mutant, and complementary strains were prepared and adjusted to OD_{595} = 0.6. The wild-type suspension was pretreated with $\mathbf{C_{31}}$, TC (both at 2.0 × EC_{50}), or 0.5% DMSO (control) for 12 h. All suspensions were inoculated into rice leaves via the leaf-clipping method. Disease severity was assessed by measuring lesion length after 14 d, and the data were analyzed using one-way analysis of variance (ANOVA).

HR assay

The HR was assayed in *N. benthamiana* [48]. Bacterial suspensions of wild-type PXO99^A, knockout mutant, and complementary strains were adjusted to OD_{595} = 0.6 and infiltrated into the abaxial leaf surface using a needleless syringe; sterile water served as the negative control. Inoculated plants were kept in a growth chamber (day/night, 25 °C/ 20 °C, 12-h light, 60% humidity). The HR phenotype, defined as localized tissue browning and necrosis, was monitored and recorded at 24 to 72 h after inoculation. All experiments included at least 3 independent biological replicates.

Detection of hydrogen peroxide resistance

Bacterial resistance to hydrogen peroxide was assessed as previously described [49]. Cultures of the wild-type PXO99^A, knockout mutant, and complementary strains were adjusted to OD_{595} = 0.6. After a 3-fold serial dilution in sterile water, 2-μl aliquots of each dilution were spotted onto NA plates supplemented with 0.1 mM H_2O_2. Following incubation at 28 °C for 48 h, bacterial growth was evaluated.

Transcriptome profiling

Cultures of the wild-type PXO99^A and the ΔRpoA mutant were grown in NB medium to mid-log phase (OD_{595} = 0.6), and cells were harvested via centrifugation for transcriptomic analysis. Raw sequencing reads from the Illumina NovaSeq platform were subjected to quality assessment using Fast QC. Quality-filtered reads were aligned to the reference genome via Bowtie2, and alignment statistics were generated using RSeQC. Subsequent transcript assembly, genomic region mapping, read counting, and gene expression estimation were conducted with Rockhopper.

Protein purification and MST assays

The pET-28a-RpoA plasmid was transformed into *E. coli* Rosetta (DE3) cells for protein expression. Expression was induced with 0.1 mM isopropyl-β-D-thiogalactopyranoside at 37 °C for 4 h. Cells were harvested and lysed via ultrasonication, and the soluble fraction was analyzed using sodium dodecyl sulfate–polyacrylamide gel electrophoresis. The His-tagged RpoA protein was purified using a Ni–NTA affinity column (GE Healthcare, USA). Compound–protein binding affinity was measured using a Monolith NT.115 instrument (NanoTemper Technologies, Germany). Data from MST experiments were analyzed using MO. The Affinity Analysis software (version 2.2.4) was used to determine K_D. All steps were performed according to an established protocol [50].

BLI assays

The binding interactions between the compounds and RpoA were characterized by BLI. Briefly, purified RpoA (1 mg/ml) was biotinylated by incubating with 10 mM biotin for 30 min at room temperature. The sample was then desalted and immobilized on a Super Streptavidin biosensor. Real-time binding was monitored using an Octet BLI system (Forte Bio, USA) by exposing the sensor to a series of concentrations of each compound. Global fitting of the resulting binding curves was performed using the Octet Analysis Studio software to determine K_D and assess binding affinity.

Confocal microscopy and FRAP

Confocal microscopy was performed on the *Agrobacterium*-infected leaves using a Zeiss LSM900 laser scanning microscope (Zeiss, Germany). Time-lapse images were acquired over 1 to 2 min following excitation of fluorescent proteins at 488 nm. For FRAP, selected intracellular BMCs were photobleached using a 488-nm laser at 50% or 100% intensity with a 20× water immersion objective and 2.5× digital zoom. Recovery was monitored using time-lapse imaging for ≥40 frames. All images were acquired with the ZEN 3.1 software (Zeiss, Germany), and fluorescence intensities were quantified. Normalized data were plotted as recovery curves using GraphPad Prism 9.5.

In vivo assessment of treatments for rice bacterial blight

The control efficacy of the highly active compounds, $\mathbf{C_{31}}$, SA, and TC, was evaluated in vivo using an equal volume of DMSO as a negative control. In the protective assay, rice plants were sprayed with 200 μg/ml of the agents prior to clip-inoculation with *Xoo* (OD_{595} = 0.7). In the curative assay, the agents were applied 24 h postinoculation. All plants were maintained at 28 °C and 90% relative humidity for 14 d. Disease severity was scored according to the lesion length. The disease index (DI) and control efficacy (CE) were calculated using Eqs. (1) and (2), respectively:

$$\mathrm{DI}\ (\%) = \left[\sum (N \times G)/(D \times M)\right] \times 100 \quad (1)$$

$$\mathrm{CE}\ (\%) = \left[(C - T)/C\right] \times 100 \quad (2)$$

where N is the number of leaves in a given grade, G is the corresponding grade value, D is the total number of diseased leaves, M is the highest grade value, C is the disease index of the control group, and T is the disease index of the treated group.

Phytotoxicity assay on target plants

Rice plants were evenly sprayed with $\mathbf{C_{31}}$ or TC (500 μg/ml), using a 0.4% DMSO solution as a negative control. After treatment, the plants were placed in a greenhouse at 28 °C and 90% relative humidity for 7 d. Leaf damage and phytotoxic symptoms

were monitored and recorded daily throughout the observation period.

Statistical analysis and reproducibility

Data analysis was performed using IBM SPSS Statistics 24, Origin 2024, and GraphPad Prism 9.5. All quantitative data are expressed as mean ± standard error from at least 3 independent experimental replicates. The specific sample sizes (n) for each experiment are shown in the corresponding figure legends. For comparisons between the 2 groups, an unpaired 2-tailed Student t test was used. For comparisons across multiple groups, a one-way ANOVA was applied, followed by the least significant difference post hoc test for specific pairwise comparisons. All tests were 2-tailed.

Acknowledgments

Funding: This work was supported by the National Natural Science Foundation of China (No. 32472604), the Guizhou Provincial Science & Technology Achievements Transformation Project (Qiankehechengguo[2025]zhongda004), and the Scientific Research Innovation Team of Guizhou University (No. 202403).

Author contributions: Conceptualization: R.S. and D.H. Methodology: X.W. Investigation: X.W. and J.L. Visualization: X.W. Formal analysis: X.W., T.L., and C.Z. Writing—original draft: X.W. and T.L. Writing—review and editing: R.S. and D.H. Supervision: R.S. and D.H. Funding acquisition: R.S. and D.H. Project administration: R.S. and D.H. All authors reviewed and approved the final version of the manuscript.

Competing interests: The authors declare that they have no competing interests.

Data Availability

All data needed to evaluate the conclusions in the paper are present in the paper and/or the Supplementary Materials. All other relevant source data are available from the corresponding authors upon request.

Supplementary Materials

Supplementary Text
Figs. S1 to S131
Tables S1 to S3
Dataset S1
Videos S1 and S2
References [52–57]

References

1. Jeon S, Jeon Y, Lim J-Y, Kim Y, Cha B, Kim W. Emerging regulatory mechanisms and functions of biomolecular condensates: Implications for therapeutic targets. *Signal Transduct Target Ther*. 2025;10(1):4.
2. Brangwynne CP, Eckmann CR, Courson DS, Rybarska A, Hoege C, Gharakhani J, Jülicher F, Hyman AA. Germline P granules are liquid droplets that localize by controlled dissolution/condensation. *Science*. 2009;324(5935):1729–1732.
3. Yin LM, Li XY, Zhao CN, Song RJ, Song BA. CGMMV capsid protein hijacks host pro-viral factors to generate condensates and remodel photosynthesis: Strategic antiviral protocol. *Sci Bull*. 2025;70(23):3952–3956.
4. Zan NN, Li J, Yao JH, Wu S, Li JZ, Chen FF, Song BA, Song RJ. Rational design of phytovirucide inhibiting nucleocapsid protein aggregation in tomato spotted wilt virus. *Nat Commun*. 2025;16(1):2034.
5. Li HH, Ernst C, Kolonko-Adamska M, Greb-Markiewicz B, Man J, Parissi V, Ng BW-L. Phase separation in viral infections. *Trends Microbiol*. 2022;30(12):1217–1231.
6. Monterroso B, Margolin W, Boersma AJ, Rivas G, Poolman B, Zorrilla S. Macromolecular crowding, phase separation, and homeostasis in the orchestration of bacterial cellular functions. *Chem Rev*. 2024;124(4):1899–1949.
7. Hoang Y, Azaldegui CA, Dow RE, Ghalmi M, Biteen JS, Vecchiarelli AG. An experimental framework to assess biomolecular condensates in bacteria. *Nat Commun*. 2024;15(1):3222.
8. Zhao YX, Dai EH, Zhang MT, Wu YF, Sun DJ, Ding JB. Mechanisms and pathological significance of liquid-liquid phase separation in bacteria. *FASEB J*. 2025;39(18):Article e71074.
9. Henry JT, Crosson S. Chromosome replication and segregation govern the biogenesis and inheritance of inorganic polyphosphate granules. *Mol Biol Cell*. 2013;24(20):3177–3186.
10. Ramm B, Schumacher D, Harms A, Heermann T, Klos P, Mueller F, Schwille P, Soegaard-Andersen L. Biomolecular condensate drives polymerization and bundling of the bacterial tubulin FtsZ to regulate cell division. *Nat Commun*. 2023;14(1):3825.
11. Liang QY, Peng NN, Xie Y, Kumar N, Gao WB, Miao YS. MolPhase, an advanced prediction algorithm for protein phase separation. *EMBO J*. 2024;43(9):1898–1918.
12. Sneideris T, Erkamp NA, Ausserwoger H, Saar KL, Welsh TJ, Qian DY, Katsuya-Gaviria K, Johncock MLLY, Krainer G, Borodavka A, et al. Targeting nucleic acid phase transitions as a mechanism of action for antimicrobial peptides. *Nat Commun*. 2023;14(1):7170.
13. Liu M, Wu CJ, Wang R, Qiu JM, She ZT, Qu JN, Xia J. Modulating liquid–liquid phase separation of Nck adaptor protein against enteropathogenic *Escherichia coli* infection. *ACS Cent Sci*. 2023;9(12):2358–2368.
14. Timilsina S, Potnis N, Newberry EA, Liyanapathiranage P, Iruegas-Bocardo F, White FF, Goss EM, Jones JB. *Xanthomonas* diversity, virulence and plant–pathogen interactions. *Nat Rev Microbiol*. 2020;18(8):415–427.
15. Kaur A, Minsavage GV, Potnis N, Jones JB, Goss EM. Evolution of copper resistance in *Xanthomonas euvesicatoria* pv. *perforans* population. *mSystems*. 2024;9(12):e0142724.
16. Xu Y, Zhu X-F, Zhou M-G, Kuang J, Zhang Y, Shang Y, Wang J-X. Status of streptomycin resistance development in *Xanthomonas oryzae* pv. *oryzae* and *Xanthomonas oryzae* pv. *oryzicola* in China and their resistance characters. *J Phytopathol*. 2010;158(9):601–608.
17. Srinivasulu C, Ramgopal M, Ramanjaneyulu G, Anuradha CM, Chitta SK. Syringic acid (SA)—A review of its occurrence, biosynthesis, pharmacological and industrial importance. *Biomed Pharmacother*. 2018;108:547–557.
18. Shimsa S, Mondal S, Mini S. Syringic acid: A promising phenolic phytochemical with extensive therapeutic applications. *Funct Food Prod R&D*. 2024;1(5):1–14.
19. Zheng YP, Wu SK, Li JZ, Shen ZJ, Li J, Wu ZX, Hu DY, Song BA. Development of dual-function disulfaneyl oxadiazole

bactericides by structurally incorporating β-carboline moieties. *Bioorg Chem*. 2025;162:Article 108606.
20. Lu HX, Shen ZJ, Xu YJ, Wu LJ, Hu DY, Song RJ, Song BA. Immune mechanism of ethylicin-induced resistance to *Xanthomonas oryzae* pv. *oryzae* in rice. *J Agric Food Chem*. 2023;71(1):288–299.
21. Li JZ, Liu Q, Li S, Zeng L, Yao JH, Li HD, Shen ZJ, Lu FN, Wu ZX, Song BA, et al. Design, synthesis, antibacterial activity, and mechanisms of novel benzofuran derivatives containing disulfide moieties. *J Agric Food Chem*. 2024;72(18): 10195–10205.
22. Koparir M, Cetin A, Cansiz A. 5-Furan-2-yl[1,3,4]oxadiazole-2-thiol, 5-furan-2-yl-4*H*-[1,2,4]triazole-3-thiol and their thiol-thione tautomerism. *Molecules*. 2005;10(2):475–480.
23. Nguyen VT, Haug GC, Nguyen VD, Vuong NTH, Karki GB, Arman HD, Larionov OV. Functional group divergence and the structural basis of acridine photocatalysis revealed by direct decarboxysulfonylation. *Chem Sci*. 2022;13(14): 4170–4179.
24. Watanabe N, Lam E. The hypersensitive response in plant disease resistance. *Annu Rev Plant Physiol Plant Mol Biol*. 1997;48:575–607.
25. Singh A, Gupta R, Tandon S, Pandey R. Anti-biofilm and anti-virulence potential of 3,7-dimethyloct-6-enal derived from citrus hystrix against bacterial blight of rice caused by *Xanthomonas oryzae* pv. *oryzae*. *Microb Pathog*. 2018;115: 264–271.
26. Liang XY, Yu XY, Dong WX, Guo SJ, Xu S, Wang JX, Zhou MG. Two thiadiazole compounds promote rice defence against *Xanthomonas oryzae* pv. *oryzae* by suppressing the bacterium's production of extracellular polysaccharides. *Mol Plant Pathol*. 2015;16(8):882.
27. Cotter PA, DiRita VJ. Bacterial virulence gene regulation: An evolutionary perspective. *Ann Rev Microbiol*. 2000;54:519–565.
28. Li R-F, Ren P-D, Liu Q-Q, Yao J-L, Wu L, Zhu G-N, Xian X-Y, Tang J-L, Lu G-T. McvR, a single domain response regulator regulates motility and virulence in the plant pathogen *Xanthomonas campestris*. *Mol Plant Pathol*. 2022;23(5): 649–663.
29. Flemming HC, Wingender J. The biofilm matrix. *Nat Rev Microbiol*. 2010;8(9):623–633.
30. Kohga H, Lertpreedakorn N, Miyazaki R, Wu SX, Hosoda K, Tanaka H, Takahashi YS, Yoshikaie K, Kuruma Y, Shigematsu H, et al. Phage lysis protein Lys^M acts as a wedge to block MurJ conformational changes. *Sci Adv*. 2025;11(41):eady8083.
31. Interlandi G, Thomas WE. Mechanism of allosteric propagation across a β-sheet structure investigated by molecular dynamics simulations. *Proteins*. 2016;84(7):990–1008.
32. Ma KY, Temiakov D, Jiang ML, Anikin M, McAllister WT. Major conformational changes occur during the transition from an initiation complex to an elongation complex by T7 RNA polymerase. *J Biol Chem*. 2002;277(45):43206–43215.
33. Nandana V, Schrader JM. Roles of liquid-liquid phase separation in bacterial RNA metabolism. *Curr Opin Microbiol*. 2021;61:91–98.
34. Meszaros B, Erdos G, Dosztanyi Z. IUPred2A: Context-dependent prediction of protein disorder as a function of redox state and protein binding. *Nucleic Acids Res*. 2018;46(W1):W329–W337.
35. Paget MS, Helmann JD. The σ^{70} family of sigma factors. *Genome Biol*. 2003;4(1):203.
36. Ross W, Schneider DA, Paul BJ, Mertens A, Gourse RL. An intersubunit contact stimulating transcription initiation by *E. coli* RNA polymerase: Interaction of the α C-terminal domain and σ region 4. *Genes Dev*. 2003;17(10):1293–1307.
37. Chen H, Tang H, Ebright RH. Functional interaction between RNA polymerase α subunit C-terminal domain and σ^{70} in UP-element- and activator-dependent transcription. *Mol Cell*. 2003;11(6):1621–1633.
38. Song RJ, Zhang YP, Lu P, Wu J, Li QX, Song BA. Status and perspective on green pesticide utilizations and food security. *Annu Rev Food Sci Technol*. 2024;15(1):473–493.
39. Ide S, Imai R, Ochi H, Maeshima K. Transcriptional suppression of ribosomal DNA with phase separation. *Sci Adv*. 2020;6(42):eabb5953.
40. Weng XL, Bohrer CH, Bettridge K, Lagda AC, Cagliero C, Jin DJ, Xiao J. Spatial organization of RNA polymerase and its relationship with transcription in *Escherichia coli*. *Proc Natl Acad Sci USA*. 2019;116(40):20115–20123.
41. Endesfelder U, Finan K, Holden SJ, Cook PR, Kapanidis AN, Heilemann M. Multiscale spatial organization of RNA polymerase in *Escherichia coli*. *Biophys J*. 2013;105(1):172–181.
42. Xu ZZ, Wu GC, Wang B, Zhao YC, Liu FQ. TrpR-like protein PXO_00831, regulated by the sigma factor RpoD, is involved in motility, oxidative stress tolerance, and virulence in *Xanthomonas oryzae* pv. *Oryzae*. *Phytopathology*. 2023;113(2):170–182.
43. Xu ZZ, Wu GC, Wang B, Guo BD, Sheng C, Zhao YY, Tang B, Zhao YC, Liu FQ. Sigma factor 70 RpoD contributes to virulence by regulating cell motility, oxidative stress tolerance, and manipulating the expression of *hrpG* and *hrpX* in *Xanthomonas oryzae* pv. *oryzae*. *J Integr Agr*. 2025;24(5): 1844–1859.
44. Ladouceur AM, Parmar BS, Biedzinski S, Walla J, Tope SG, Cohn D, Kim A, Soubry N, Reyes-Lamothe R, Weber SC. Clusters of bacterial RNA polymerase are biomolecular condensates that assemble through liquid-liquid phase separation. *Proc Natl Acad Sci USA*. 2020;117(31): 18540–18549.
45. Azaldegui CA, Vecchiarelli AG, Biteen JS. The emergence of phase separation as an organizing principle in bacteria. *Biophys J*. 2021;120(7):1123–1138.
46. Wang B, Wu GC, Li KH, Ling J, Zhao YC, Liu FQ. A glycoside hydrolase family 99-like domain-containing protein modifies outer membrane proteins to maintain *Xanthomonas* pathogenicity and viability in stressful environments. *Phytopathology*. 2021;111(6):929–939.
47. Yang B, Bogdanove A. Inoculation and virulence assay for bacterial blight and bacterial leaf streak of rice. *Methods Mol Biol*. 2013;956:249–255.
48. Li RM, Wang S, Sun RH, He X, Liu YT, Song CF. *Xanthomonas oryzae* pv. *oryzae* type III effector PthXo3JXOV suppresses innate immunity, induces susceptibility and binds to multiple targets in rice. *FEMS Microbiol Lett*. 2018;365(7):fny037/1–fny037/9.
49. Qian GL, Liu CH, Wu GC, Yin FQ, Zhao YC, Zhou YJ, Zhang YB, Song ZW, Fan JQ, Hu BS, et al. AsnB, regulated by diffusible signal factor and global regulator Clp, is involved in aspartate metabolism, resistance to oxidative stress and virulence in *Xanthomonas oryzae* pv. *oryzicola*. *Mol Plant Pathol*. 2013;14(2):145–157.
50. Zhang AW, Zhang HZ, Wang RH, He GF, Song BA, Song RJ. Bactericidal bissulfone B_7 targets bacterial pyruvate kinase to

impair bacterial biology and pathogenicity in plants. *Sci China Life Sci*. 2024;67(2):391–402.
51. Jiang S, Li H, Zhang L, Mu W, Zhang Y, Chen T, Wu J, Tang H, Zheng S, Liu Y, et al. Generic Diagramming Platform (GDP): A comprehensive database of high-quality biomedical graphics. *Nucleic Acids Res*. 2025;53(D1): D1670–D1676.
52. Wu SK, Shi J, Chen JX, Hu DY, Zang LS, Song BA. Synthesis, antibacterial activity, and mechanisms of novel 6-sulfonyl-1,2,4-triazolo[3,4-b][1,3,4] thiadiazole derivatives. *J Agric Food Chem*. 2021;69(16):4645–4654.
53. Zou H-S, Yuan L, Guo W, Li Y-R, Che Y-Z, Zou L-F, Chen G-Y. Construction of a Tn5-tagged mutant library of *Xanthomonas oryzae* pv. *oryzicola* as an invaluable resource for functional genomics. *Curr Microbiol*. 2011;62(3):908–916.
54. Wang XG, Li SY, Liu DY, Li HD, Hu DY, Song RJ. Novel aurone-derived piperazine sulfonamides: Development and mechanisms of action as immunostimulants against plant bacterial diseases. *Pestic Biochem Physiol*. 2024;202:Article 105955.
55. Liu H-W, Ji Q-T, Ren G-G, Wang F, Su F, Wang P-Y, Zhou X, Wu Z-B, Li Z, Yang S. Antibacterial functions and proposed modes of action of novel 1,2,3,4-tetrahydro-β-carboline derivatives that possess an attractive 1,3-diaminopropan-2-ol pattern against rice bacterial blight, kiwifruit bacterial canker, and citrus bacterial canker. *J Agric Food Chem*. 2020;68(45):12558–12568.
56. Liu HW, Su SS, Ma SY, Li T, Fang W, Ding Y, Liu S-T, Zhang J-R, Xiang H-M, Zhou X, et al. Discovery and structural optimization of 1,2,3,4-tetrahydro-β-carbolines as novel reactive oxygen species inducers for controlling intractable plant bacterial diseases. *J Agric Food Chem*. 2023;71(29):11035–11047.
57. Yang JH, Liu KJ, Chen YZ, Ye HJ, Hao GF, Du FP, Wang PY. A supramolecular bactericidal material for preventing and treating plant-associated biofilms. *Nat Commun*. 2025;16(1):2627.